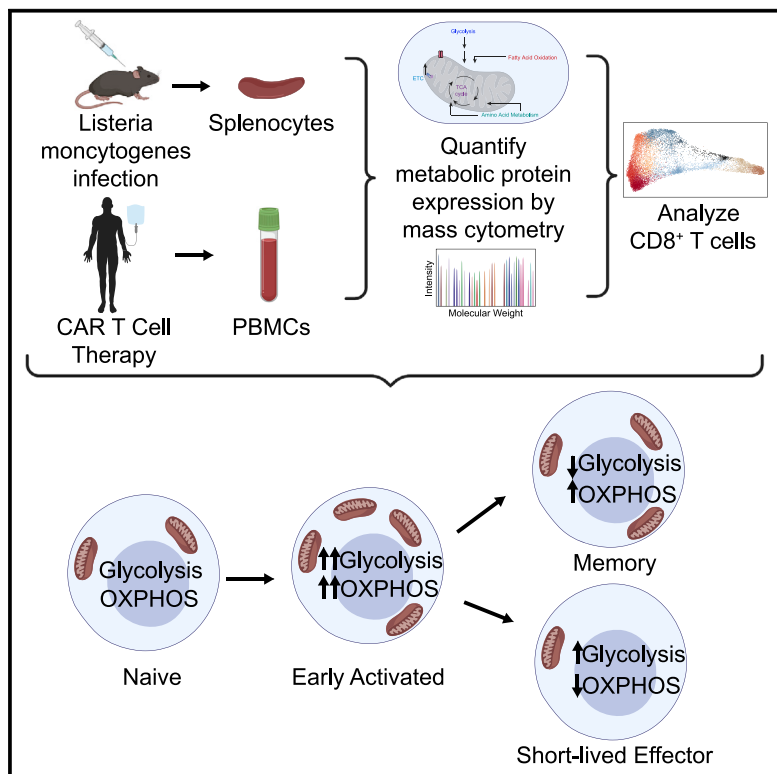


# Immunity

## Single-cell analysis by mass cytometry reveals metabolic states of early-activated CD8<sup>+</sup> T cells during the primary immune response

### Graphical Abstract



### Authors

Lauren S. Levine,  
Kamir J. Hiam-Galvez,  
Diana M. Marquez, ...,  
Olalekan O. Oluwole,  
Jeffrey C. Rathmell, Matthew H. Spitzer

### Correspondence

[matthew.spitzer@ucsf.edu](mailto:matthew.spitzer@ucsf.edu)

### In brief

Levine, Hiam-Galvez, et al. develop a mass-cytometry-based approach to quantify metabolic protein expression in single cells *in vivo*, revealing a distinct metabolic state early after CD8<sup>+</sup> T cell activation characterized by simultaneous expression of glycolytic and oxidative proteins. This approach provides a resource for the study of metabolic regulation across a variety of applications.

### Highlights

- A mass cytometry approach quantifies metabolic proteins in single cells *in vivo*
- Early-activated T cells exhibit simultaneous peak oxidative and glycolytic activity
- CD8<sup>+</sup> T cells transit through this transient state prior to differentiation
- CAR T cells exhibit an analogous transient program upon infusion into patients



## Resource

# Single-cell analysis by mass cytometry reveals metabolic states of early-activated CD8<sup>+</sup> T cells during the primary immune response

Lauren S. Levine,<sup>1,2,3,4,5,6,9</sup> Kamir J. Hiam-Galvez,<sup>1,2,3,4,5,9</sup> Diana M. Marquez,<sup>1,2,3,4,5</sup> Iliana Tenvooren,<sup>1,2,3,4,5</sup> Matthew Z. Madden,<sup>7</sup> Diana C. Contreras,<sup>7</sup> Debolanle O. Dahunsi,<sup>7</sup> Jonathan M. Irish,<sup>7</sup> Olalekan O. Oluwole,<sup>8</sup> Jeffrey C. Rathmell,<sup>7</sup> and Matthew H. Spitzer<sup>1,2,3,4,5,10,\*</sup>

<sup>1</sup>Departments of Otolaryngology-Head and Neck Cancer, University of California, San Francisco, San Francisco, CA 94143, USA

<sup>2</sup>G.W. Hooper Research Foundation, Department of Immunology and Microbiology, University of California, San Francisco, San Francisco, CA 94143, USA

<sup>3</sup>Helen Diller Family Comprehensive Cancer Center, University of California, San Francisco, San Francisco, CA 94158, USA

<sup>4</sup>Chan Zuckerberg Biohub, San Francisco, CA 94158, USA

<sup>5</sup>Parker Institute for Cancer Immunotherapy, San Francisco, CA 94129, USA

<sup>6</sup>Department of Medicine, University of California, San Francisco, San Francisco, CA 94143, USA

<sup>7</sup>Vanderbilt Center for Immunobiology, Department of Pathology, Microbiology, and Immunology, Vanderbilt University Medical Center, Nashville, TN 37232, USA

<sup>8</sup>Department of Medicine, Division of Hematology/Oncology, Vanderbilt University Medical Center, Nashville, TN 37232, USA

\*These authors contributed equally

<sup>10</sup>Lead contact

\*Correspondence: matthew.spitzer@ucsf.edu

<https://doi.org/10.1016/j.immuni.2021.02.018>

## SUMMARY

Memory T cells are thought to rely on oxidative phosphorylation and short-lived effector T cells on glycolysis. Here, we investigated how T cells arrive at these states during an immune response. To understand the metabolic state of rare, early-activated T cells, we adapted mass cytometry to quantify metabolic regulators at single-cell resolution in parallel with cell signaling, proliferation, and effector function. We interrogated CD8<sup>+</sup> T cell activation *in vitro* and in response to *Listeria monocytogenes* infection *in vivo*. This approach revealed a distinct metabolic state in early-activated T cells characterized by maximal expression of glycolytic and oxidative metabolic proteins. Cells in this transient state were most abundant 5 days post-infection before rapidly decreasing metabolic protein expression. Analogous findings were observed in chimeric antigen receptor (CAR) T cells interrogated longitudinally in advanced lymphoma patients. Our study demonstrates the utility of single-cell metabolic analysis by mass cytometry to identify metabolic adaptations of immune cell populations *in vivo* and provides a resource for investigations of metabolic regulation of immune responses across a variety of applications.

## INTRODUCTION

Understanding the regulatory mechanisms underlying immune responses is crucial to developing more rationally designed treatment strategies for acute and chronic infections, autoimmune diseases, and malignancy (Buck et al., 2017). CD8<sup>+</sup> T cells, when activated, expand and differentiate into potent short-lived effector cells (SLECs) as well as long-term memory cells, which can confer durable protection against reinfection and cancer relapse (Badovinac et al., 2007; Callahan et al., 2016; Restifo et al., 2012). The former mediate primary adaptive immune responses against pathogens through the release of cytotoxic granules and pro-inflammatory cytokines (Araki et al., 2010; Pearce et al., 2009). In contrast, long-lived memory cells remain quiescent until re-encountering antigen, upon which

they rapidly mediate secondary immune responses (Gerriets and Rathmell, 2012). The field of immunometabolism provides critical insight into these processes, revealing a complex regulatory interplay of signaling, metabolic, and epigenetic adaptations during CD8<sup>+</sup> T cell differentiation (Olenchock et al., 2017; Zhang and Romero, 2018).

Upon activation, effector CD8<sup>+</sup> T cells undergo clonal expansion, necessitating as many as 20 replication cycles to generate sufficient daughter cells to clear pathogens (Badovinac et al., 2007). This process is energetically costly and requires rapid ATP production for the biosynthesis of essential building blocks (Zhang and Romero, 2018). Previous studies suggest that the exit from quiescence is supported by a dramatic metabolic shift from oxidative phosphorylation (OXPHOS) in naive cells, fueled by beta-oxidation of long-chain fatty acids (LCFAs), to aerobic



glycolysis in SLECs, characterized by lactate production in the setting of adequate oxygen (Menk et al., 2018a; 2018b; Wang et al., 2011). This metabolic conversion permits continued cycling through the pentose phosphate pathway and thus generation of intermediates necessary for nucleic acid and lipid biosynthesis. This adaptation also circumvents negative feedback induced by the accumulation of pyruvate and acetyl-coenzyme A (acetyl-CoA) (Lee et al., 2014; Zhang and Romero, 2018). Additional feed-forward mechanisms supporting this process include the activation of transcription factors downstream of phosphoinositide 3-kinase (PI3K) signaling. For instance, hypoxia inducible factor 1 (HIF1 $\alpha$ ) mediates the increased expression of nutrient receptors, including glucose transporter 1 (Glut1), the main point of entry for glucose into T cells (Wang et al., 2011).

Meanwhile, the transition to the memory T cell fate is associated with mitochondrial biogenesis driven by AMPK (Borges da Silva et al., 2018; Buck et al., 2016; D'Souza et al., 2007; Maciver et al., 2011; Pearce et al., 2009; Rolf et al., 2013), which is mediated by peroxisome-proliferator-activated receptor gamma coactivator 1-alpha (PGC1 $\alpha$ ) (Andrejeva and Rathmell, 2017; Menk et al., 2018a). This tightly regulated metabolic shift results in an LCFA-fueled oxidative program characterized by increased mitochondrial mass (Buck et al., 2016). This property of memory cells confers additional oxidative potential, known as spare respiratory capacity (SRC), to permit more rapid recall during secondary immune responses (van der Windt et al., 2012).

While many studies of bulk T cell populations suggest that a reciprocal, tightly regulated relationship exists between OXPHOS and glycolysis and the signaling cascades that regulate these pathways, their precise interactions in individual cells have yet to be elucidated. Moreover, the regulation of metabolic machinery in rare, early-activated T cells remains poorly understood. The early stages of infection lead to antigen-specific CD8 $^{+}$  T cells acquiring transient cell states preceding differentiation into effector subsets, but determining precisely how these intermediate stages of differentiation metabolically orchestrate rapid proliferation and differentiation has remained technically challenging (Joshi et al., 2007; Kalia et al., 2010; Obar and Le-françois, 2010). Advances in single-cell analysis have enabled studies of signaling and effector programs in T cells at high resolution (Krishnaswamy et al., 2014; Mingueneau et al., 2014). Analogous studies of T cell metabolic regulation would likely provide new insights. For instance, a study utilizing stable isotope tracing in activated T cells found that OXPHOS may be a prominent in effector T cells *in vivo* (Ma et al., 2019). However, in the absence of single-cell resolution, it remains unclear whether the same cells are responsible for both OXPHOS and glycolysis or, alternatively, whether individual cells already differentiate and preferentially utilize one pathway versus the other during the effector phase. Many of the regulatory mechanisms that govern cellular metabolism are post-transcriptional and therefore not directly measurable by RNA sequencing (Andrejeva and Rathmell, 2017). Moreover, as gene expression is not always tightly associated with protein expression (Vogel and Marcotte, 2012), proteomic approaches afford unique opportunities to assess the integrated functional programs within individual cells.

Mass cytometry utilizes metal-tagged antibodies to directly measure over 40 proteins simultaneously in individual cells (Bandura et al., 2009; Bendall et al., 2011). This approach has

permitted characterization of various aspects of cellular behavior, including phenotype, signaling (Bodenmiller et al., 2012), proliferation (Good et al., 2019), and chromatin state (Cheung et al., 2018). Here, we adapted this platform to measure expression levels of enzymes and transporters involved in metabolic checkpoints. We integrated direct quantitative evaluation of the signaling cues thought to mediate their regulation along with proteins indicative of CD8 $^{+}$  T cell fate and function. This approach was used to interrogate key inflection points of the CD8 $^{+}$  T cell response to *Listeria monocytogenes* infection (*Listeria monocytogenes* expressing whole cytoplasmic ovalbumin [Lm-OVA]), a well-characterized model of CD8 $^{+}$  T cell differentiation (Ahmed and Gray, 1996; Badovinac et al., 2007; Harty and Badovinac, 2002; Kaech and Ahmed, 2001; McGregor et al., 1970; Shen et al., 1998; Wherry and Ahmed, 2004), revealing a distinct metabolic state in early-activated T cells. The single-cell mass cytometry approach presented here constitutes a resource for investigating cellular metabolic adaptations *in vivo* across a broad array of applications.

## RESULTS

### Mass cytometry permits high-dimensional quantification of metabolic regulators in single CD8 $^{+}$ T cells

T cell differentiation requires the coordinated interplay of signaling and metabolic pathways, including the increased expression of rate-limiting enzymes and regulatory switches. The transition to aerobic glycolysis in SLECs is mediated by co-stimulatory signaling through CD28 via the AKT/PI3K pathway (Pollizzi et al., 2015; Wang et al., 2011); therefore, we measured the downstream intermediates mTOR, pS6, p4EBP1, and HIF1 $\alpha$  (Figure 1A; Table S1). Signaling through this pathway promotes glucose uptake through the Glut1 receptor and the transcription of glycolytic enzymes (Dennis et al., 2012), including glyceraldehyde-3-phosphate dehydrogenase (GADPH) (Figure 1B), a critical metabolic switch implicated in glycolytic activity, which we also quantified.

To investigate how the TCA cycle is regulated in activated T cells, we evaluated the expression of citrate synthase (CS) (Figure 1B; Table S1), the first step of the cycle, which is directly regulated by the NAD $^{+}$  to NADH ratio, the ADP/ATP ratio, and succinyl-CoA levels (Wiegand and Remington, 1986). As branched-chain amino acid metabolism has been demonstrated to be critical for effective T cell activation (Ren et al., 2017), we sought to understand this process by measuring the large neutral amino acid transporter (LAT1) chaperone CD98 (Figure 1A; Table S1), a key mediator of the import of these essential nutrients (Hayashi et al., 2013; Nii et al., 2001; Sinclair et al., 2013).

Previous work has described a reciprocal relationship between aerobic glycolysis and OXPHOS, the latter of which is associated with memory T cell differentiation. Therefore, we sought to understand this regulation at the single-cell level by measuring carnitine palmitoyltransferase 1A (CPT1a), an enzyme that catalyzes the transport of LCFA from the cytoplasm to the mitochondria and is critical for memory T cell function (van der Windt et al., 2012). Additionally, we measured the mitochondrial trifunctional complex, also known as hydroxyacyl-CoA

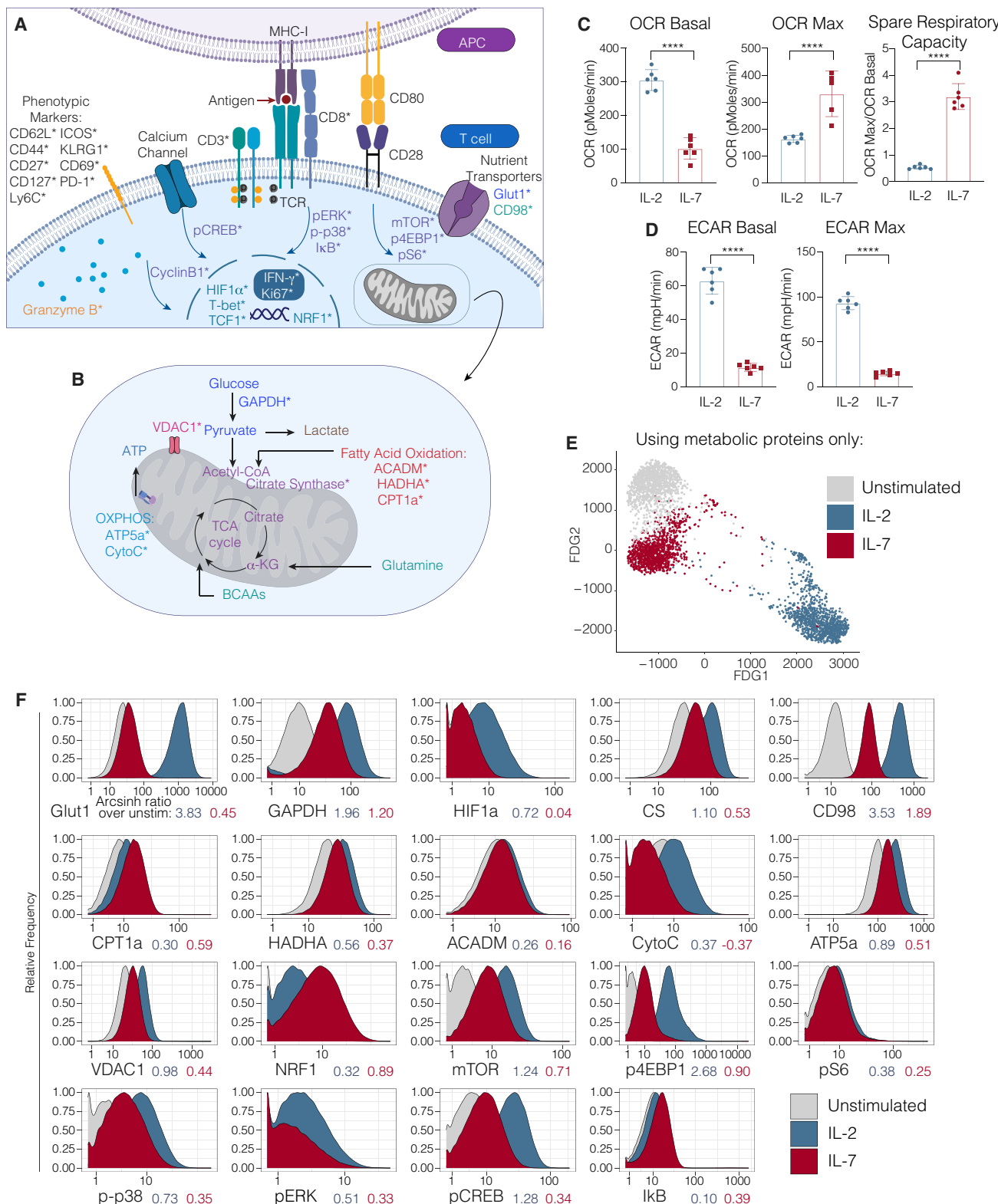


**Figure 1. Querying the integrated functional program of CD8<sup>+</sup> T cell activation**

Panel schematic depicting signaling, metabolic, effector, and phenotypic targets interrogated by mass cytometry.

(A and B) Cell surface, cytosolic, and nuclear markers (A) and mitochondrial markers (B). Markers directly measured by mass cytometry are demarcated by an asterisk.

(legend continued on next page)

dehydrogenase (HADHA), which catalyzes the final three steps of LCFA oxidation to acetyl-CoA in the mitochondria (Carpenter et al., 1992). As the role of beta-oxidation of medium-chain fatty acids in T cell function has not been extensively evaluated (Howie et al., 2018), we also measured the expression of medium-chain acyl-CoA dehydrogenase (ACADM), an essential enzyme that catalyzes the initial step of this process (Figure 1B; Table S1). Moreover, we measured key components of the electron transport chain, including cytochrome c (CytoC) and ATP synthase (ATP5a) (Figure 1B; Table S1). To understand the counterregulatory processes governing OXPHOS activity and overall energy, we measured voltage-dependent ion channel 1 (VDAC1), a critical regulator controlling cytoplasmic-mitochondrial cross-talk (Figure 1B; Table S1; Cunningham et al., 2018; Tarze et al., 2007).

The cell signaling pathways that mediate mitochondrial fusion and biogenesis include mitogen-activated protein kinase (MAPK) and nuclear factor κB (NF-κB), which are activated during T cell priming (Menk et al., 2018a; Teijeira et al., 2018; Laforgue et al., 2016); therefore, we measured the levels of phosphorylated ERK (pERK) and p-p38 MAPKs in addition to the total levels of NF-κB inhibitor alpha (IkB $\alpha$ ). Calcium signaling, triggered by T cell receptor (TCR) ligation, has also been implicated in this process (Feske, 2007; Fracchia et al., 2013). Therefore, we additionally measured pCREB levels (Figure 1A; Table S1).

It has been proposed that the activity of metabolic pathways induces epigenetic regulators, such as Ezh2, which directly impact T cell fate and function (Chiscolm et al., 2017; Gray et al., 2017). Therefore, we included a full range of well-characterized surface markers and transcription factors to subset T cells into naive, central memory, effector memory, and terminal effector populations. To measure the impact of all of these factors on T cell proliferation during clonal expansion, we measured expression of cyclinB1 and Ki67. Finally, to assess production of cytotoxic mediators, we also measured granzyme B (Figure 1A; Table S1).

### Mass cytometry recapitulates metabolic phenotypes of CD8 $^{+}$ T cell differentiation *in vitro*

In order to query the metabolic program underlying antigen-specific CD8 $^{+}$  T cell activation *in vitro*, we first stimulated TCR transgenic OT-1 splenocytes in the presence of their cognate antigen (the SIINFEKL peptide from ovalbumin) and interleukin-2 (IL-2) for 72 h. After this initial priming period, antigen was removed, and cells were polarized in IL-2 or IL-7 for an additional 4 days to generate effector (OT-1 $_{\text{eff}}$ ) or central memory (OT-1 $_{\text{mem}}$ ) cells, as described previously (Carrio et al., 2004; Pearce et al., 2009; van der Windt et al., 2012). We analyzed the resulting cells by mass cytometry and real-time metabolic profiling by Seahorse assay (Figures 1C and S1B–S1D). In keeping with prior studies (Pearce et al., 2009; van der Windt et al., 2012), OT-1 $_{\text{eff}}$  cells ex-

hibited higher rates of extracellular acidification associated with glycolytic activity (Figure 1C), while OT-1 $_{\text{mem}}$  cells possessed marked SRC, though their basal oxygen consumption rate was lower (Figure 1D; Raud et al., 2018). Also consistent with previous reports (Raud et al., 2018), OT-1 $_{\text{mem}}$  exhibited an increase in basal oxygen consumption rate (OCR) in the presence of palmitate as measured by extracellular flux analysis (Figures S1F and S1G), consistent with their ability to utilize fatty acid oxidation (FAO). While OT-1 $_{\text{mem}}$  once again exhibited SRC, the increase in OCR after the addition of fluoro-carbonyl cyanide phenylhydrazone (FCCP) was largely independent of the presence of palmitate (Figures S1F and S1G). These data indicated that while IL-7 polarized OT-1 T cells could indeed oxidize exogenous palmitate, this substrate did not greatly alter the SRC of these cells (Raud et al., 2018).

We next characterized the metabolic programs of polarized OT-1 populations by mass cytometry. We first visualized these single-cell data via dimensionality reduction, only taking into account the expression of the metabolic proteins without the use of any phenotypic markers. This analysis showed that, purely on the basis of metabolic protein expression, cells polarized in different ways that were clearly unique (Figure 1E). Moreover, to identify the relative contribution of each metabolic marker to clustering results, we repeated this analysis, each time leaving out one metabolic protein at a time (Figure S1B). The integrity of the data structure was largely maintained with each omission, demonstrating that no single protein drives the entirety of the differences (Figure S1B).

Consistent with the results of our extracellular flux analyses, OT-1 $_{\text{eff}}$  cells expressed elevated levels of glycolytic proteins at day 7 of activation, as evidenced by robust increase in expression of Glut1 and GAPDH (Figures 1F and S1A), suggestive of active glucose uptake and utilization. The expression of targets of the PI3K/mTORC1 pathway, including p4EBP1 and HIF1 $\alpha$ , were likewise elevated in OT1 $_{\text{eff}}$  cells (Figure 1F), consistent with the promotion of aerobic glycolysis. Also in keeping with previous data (Ren et al., 2017), the amino acid transporter CD98 was more highly expressed in OT1 $_{\text{eff}}$  cells relative to OT-1 $_{\text{mem}}$  cells (Figure 1F). In contrast to their effector counterparts, OT-1 $_{\text{mem}}$  cells did not demonstrate this glycolytic profile but instead increased expression of CPT1a (Figures 1F and S1A), the expression of which was therefore associated with increased SRC, but not higher basal oxygen consumption, under these conditions (Figure 1D,F). Moreover, in keeping with previous reports (Raud et al., 2018), CPT1a expression was associated with the ability of OT1 $_{\text{mem}}$  cells to metabolize exogenous palmitate, as measured by extracellular flux analysis (Figures S1F and S1G), while the latter did not account for the observed SRC, underscoring the importance of both cellular adaptations and substrate availability for cellular metabolism.

(C and D) Extracellular acidification rate (C) and oxygen consumption rate (D) of OT-1 transgenic CD8 $^{+}$  T cells stimulated and polarized with IL-2 or IL-7 and quantified by Seahorse assay. Significance analysis by Student's t test (\*\*p < 0.001). Error bars represent SEM. Data are representative of three independent experiments.

(E) Single OT-1 T cells left unstimulated (gray) or stimulated and polarized with IL-2 (blue) or IL-7 (red) visualized using a force-directed graph, taking into account only the expression of metabolic proteins (Glut1, GAPDH, HIF1 $\alpha$ , CS, CD98, CPT1a, HADHA, ACADM, CytoC, ATP5a, VDAC1, and NRF1).

(F) Mass cytometry expression profiles of key metabolic enzymes in OT-1 T cells left unstimulated (gray) or stimulated and polarized with IL-2 (blue) or IL-7 (red). Arcsinh ratios between the median expression value of each stimulated condition compared to unstimulated cells are shown below the x axis for each protein.

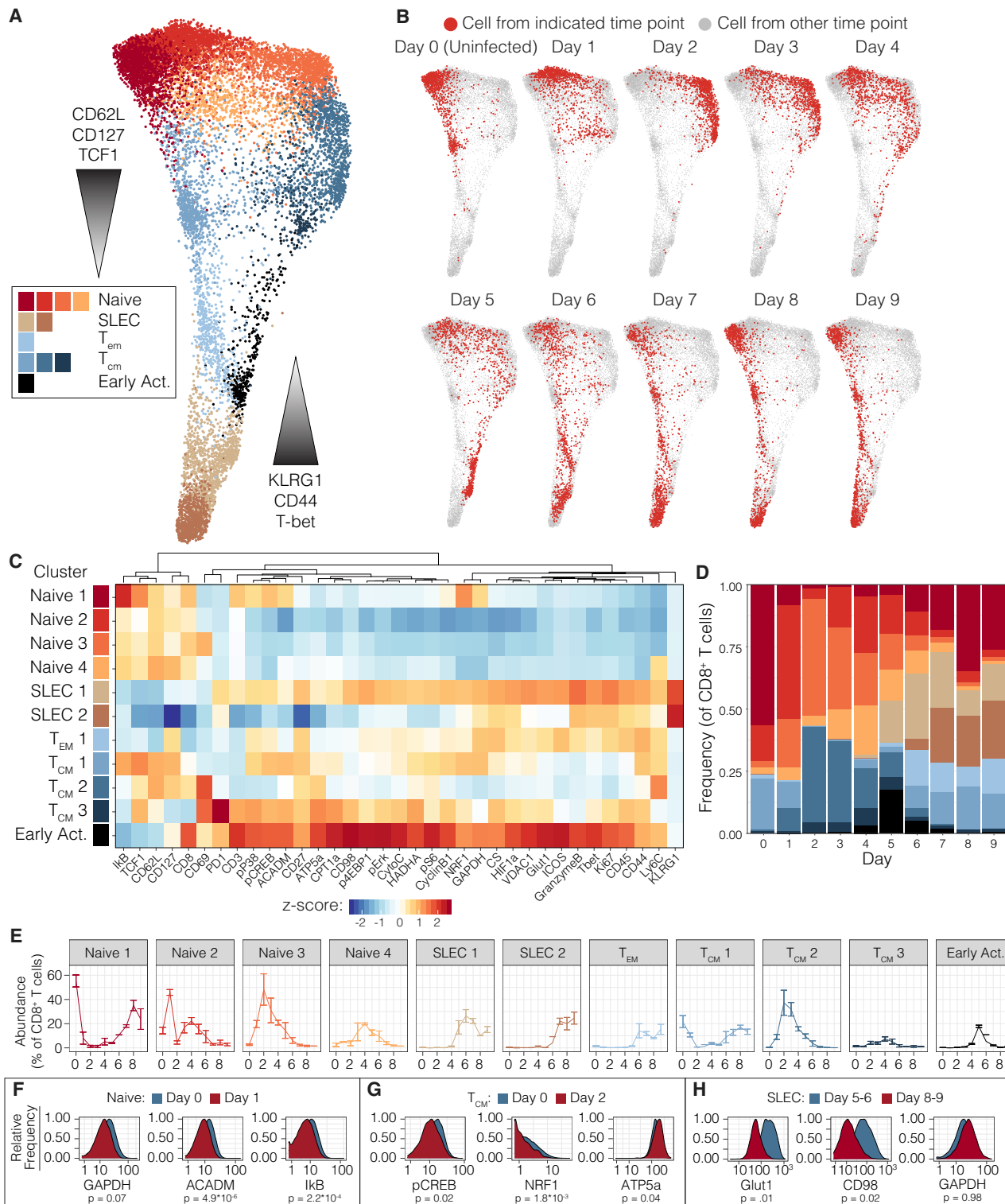


**Figure 2.** Single-cell analysis of the CD8<sup>+</sup> T cell effector program *in vivo*

(A) Pooled CD8<sup>+</sup> T cells from mice at days 0–9 of Lm-OVA infection ( $n = 2$ –3 mice per time point) clustered by phenograph and visualized by a force-directed graph.

(B) Force-directed graphs indicating cellular distribution by time point.

(legend continued on next page)

### Dynamic metabolic changes in canonical subsets of activated CD8<sup>+</sup> T cells *in vivo*

To understand the metabolic changes during CD8<sup>+</sup> T cell differentiation in a more physiologic context, we next evaluated the trajectory of the response to acute infection *in vivo*. C57BL/6 mice were infected with Lm-OVA, a well-characterized model of CD8<sup>+</sup> T cell metabolism (Buck et al., 2016; Pearce et al., 2009; van der Windt et al., 2012). Splenocytes were harvested daily over the first 9 days post-infection (p.i.) for analysis by mass cytometry. We began by performing unsupervised clustering of the CD8<sup>+</sup> T cells and visualizing them using dimensionality reduction (Figures 2A and S2A). We assigned clusters to canonical T cell differentiation states based on their expression of classical markers of CD8<sup>+</sup> T cell differentiation and investigated changes in metabolic enzyme and transporter expression over the course of the immune response. This analysis revealed considerable heterogeneity and dynamic functional changes across all major canonical T cell subsets over the course of the primary immune response to *Listeria monocytogenes* (Figures 2A and 2B).

At baseline, most naive cells were predominantly contained within cluster naive 1, characterized by the expression of ACADM, pCREB, p-p38, and NRF1 and weak expression of GAPDH (Figure 2C). However, three clusters, naive 2 and naive 3, emerged at days 1 and 2 p.i. (Figures 2D and 2E), all characterized by the decreased expression of all of the above metabolic and signaling markers (Figures 2C and S2A). Interestingly, these clusters demonstrated low IκB expression, suggestive of signaling through NF-κB pathway (Figures 2C, 2F, S2A, and S2B). While most naive T cells were contained within the naive 2 cluster at day 1 p.i. (Figures 2D and 2E), this gave way to a predominance of the naive 3 cluster at days 2 and 3 p.i. (Figures 2D and 2E). By day 4 p.i., all these clusters as well as an additional cluster, naive 4, were present in similar proportions (Figures 2D and 2E). Notably, the naive 1 cluster began to re-emerge at day 6 p.i. and ultimately dominated the naive pools from day 7 p.i. onward (Figures 2D and 2E). This predominance was associated with the involution of clusters naive 2, naive 3, and naive 4, which became nearly undetectable by day 7 p.i. (Figure 2E). These findings are consistent with activation of both bystander and antigen-specific T cells in the early stages of acute infection (Chu et al., 2013; Jiang et al., 2003) but reveal the metabolic adaptations that these cells undertake. Overall, these data support previous reports of a metabolically quiescent profile of naive T cells while identifying transitions even within these cells.

Evaluation of the central memory cells over the course of infection revealed a similar pattern, starting with cluster T<sub>CM</sub>1, characterized by intermediate expression of expected markers of LCFA and OXPHOS, including p-p38, pCREB, ACADM, HADHA, and NRF1, and dim expression of ATP5a, CPT1a, pERK, and CytoC (Figure 2C). Interestingly, this cluster also expressed GAPDH

and pS6 but dimly expressed HIF1 $\alpha$  compared to effector subsets (Figures 2C and S2A). During days 1–2 p.i., cluster T<sub>CM</sub>2 emerged (Figures 2D and 2E), which decreased expression of these metabolic and signaling factors, with only weak expression of HADHA and pS6 and increased expression of ATP5a (Figures 2C, 2G, and S2C). This cluster predominated at days 2 through 4 p.i. Notably, day 2 p.i. was also marked the emergence of cluster T<sub>CM</sub>3 (Figures 2D and 2E), defined by expression of enzymes of FAO, including CPT1a, HADHA, and ACADM, along with oxidative proteins, such as CS, ATP5a, VDAC1, and CytoC (Figures 2C and S2A). These cells also expressed less pS6 and GAPDH (Figure 2C). Commensurate with this oxidative profile, cells in this cluster also expressed p-p38, pERK, and pCREB (Figures 2C and S2A). While cells in T<sub>CM</sub>3 also demonstrated expression of downstream intermediates of the PI3K cascade, such as p4EBP1 and pS6, along with transcription factors associated with aerobic glycolysis, such as HIF1 $\alpha$ , these were associated with lower GAPDH expression (Figures 2C and S2A). This metabolically active T<sub>CM</sub> cluster was transient, completely regressing by day 7 p.i. (Figures 2D and 2E). Notably T<sub>CM</sub>1 re-emerged at day 5 p.i. and remained the predominant T<sub>CM</sub> cluster from days 6 through 9 p.i. (Figure 2D). These data confirmed the previously oxidative profile of central memory cells but also revealed dynamic metabolic changes within these subsets over the course of an immune response.

Effector memory cells (T<sub>EM</sub> cells) uniformly constituted cluster T<sub>EM</sub>1, which emerged at day 5 p.i. and maintained stable frequency through day 9 p.i. (Figures 2D and 2E). These cells demonstrated a more glycolytic metabolic profile, with increased expression of GAPDH, Glut1, and HIF1 $\alpha$  and dim oxidative and FAO marker expression (Figures 2C and S2A). Meanwhile, SLECs comprised clusters SLEC1 and SLEC2 and emerged at days 5 and 6 p.i., respectively (Figures 2D and 2E). These two clusters demonstrated distinctive metabolic phenotypes. The first population to appear, SLEC1, demonstrated expression of p4EBP1, pS6, HIF1 $\alpha$ , Glut1, and GAPDH, suggestive of a glycolytic profile (Figure 2C, 2H, S2A, S2D). Previous studies have demonstrated that early effector cells continue TCA cycle engagement fueled by the uptake of amino acids and LCFA (O'Sullivan et al., 2014; Ren et al., 2017); consistently, cells in this cluster also expressed HADHA, CD98, CS, and VDAC1 (Figures 2C, 2H, S2A, and S2D). However, ATP5a and CPT1a levels in this cluster were lower than those observed in the more active T<sub>CM</sub> clusters, such as T<sub>CM</sub>3, distinguishing them from these more classically oxidative pools (Figures 2C and S2A). In comparison, cluster SLEC2 demonstrated a more muted metabolic profile, decreasing expression of all metabolic mediators except HIF1 $\alpha$ , GAPDH, and CS, taking on the terminal glycolytic state observed in previous studies (Figures 2C, 2H, S2A, and S2D). As expected, the more metabolically active cells in cluster SLEC1 expressed higher levels of Ki67 and granzyme B

(C) Functional and phenotypic median expression profiles for each CD8<sup>+</sup> T cell cluster.

(D) Cluster proportion by time point.

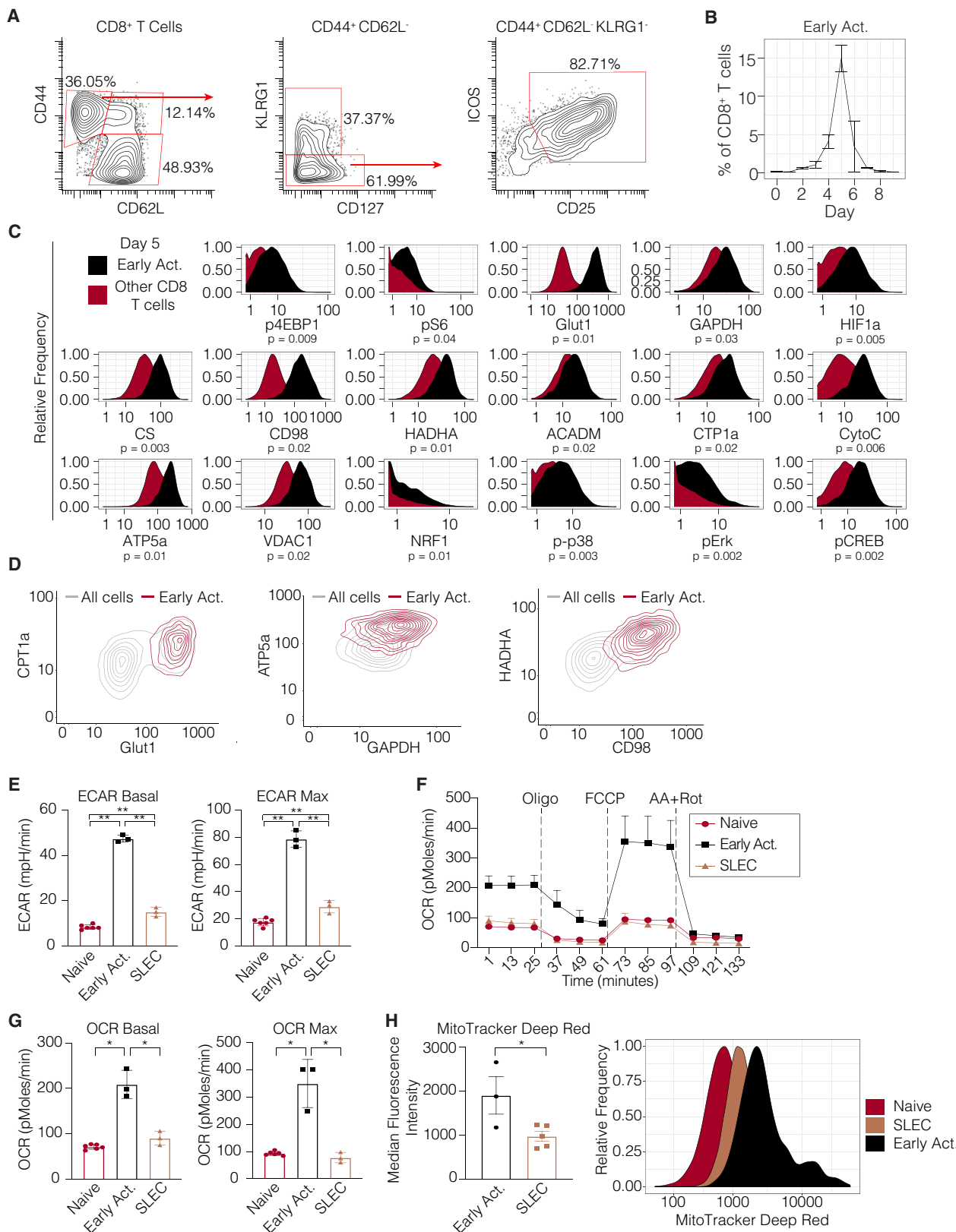
(E) Individual cluster frequency profiles at days 0–9 p.i. Error bars represent SEM.

(F) Expression profiles of metabolic and signaling in naive clusters between days 0 and 1 p.i.

(G) Expression profiles of central memory cells between days 0 and 2 p.i.

(H) Metabolic expression profiles of SLEC clusters between days 5–6 and 8–9 p.i.

Significance analysis of all medians by two-tailed Student's t test is displayed.



(legend on next page)

compared to cluster SLEC2 (Figures 2C and S2A). Taken together, these findings agreed with previous reports of a predominantly glycolytic terminal effector state.

### Early-activated T cells exhibit maximal expression of glycolytic and oxidative proteins

In addition to these well-characterized cell subsets, unsupervised high-dimensional analysis also revealed a group of early-activated T cells that emerged at day 4 post-infection (Figures 2D and 2E). These cells had high expression of Ki67, indicative of proliferation, and expressed high levels of CD44, CD27, and ICOS but low levels of CD62L (Figures 2C and S2A). This early-activated cluster was most abundant at day 5, when it comprised nearly 20% of the CD8<sup>+</sup> T cell population, and it nearly completely disappeared by day 7 (Figures 2D and 2E). As ICOS has been found to signal through the PI3K cascade (Zeng et al., 2016), we anticipated that this population would be glycolytic. Indeed, these early-activated cells expressed the highest levels of Glut1 and GAPDH across all CD8<sup>+</sup> T cells (Figure 2C). However, these cells simultaneously exhibited peak expression of oxidative markers, including CPT1a, HADHA, ACADM, and ATP5a (Figures 2C and S2A). Commensurate with this observation, the signaling program of this population was marked by maximal expression of both pS6 and pCREB as well as minimal expression of IκB, reflecting simultaneous activity of both the PI3K/mTORC1 and NF-κB pathways (Figures 2C and S2A). In contrast to SLECs and memory cells, these early-activated cells also expressed maximal expression of the amino acid transporter CD98 (Figures 2C and S2A).

Given the unique metabolic expression profile of these early-activated cells, we sought to confirm these observations through direct inspection of the primary data. We undertook further phenotypic analysis of these cells, which identified the high-affinity IL-2 receptor subunit CD25 as another surface marker co-expressed by this population of interest, consistent with their recent activation (Figure 3A). Consistent with the clustering analysis, we found that these manually gated cells peaked in frequency at day 5, followed by a rapid decline in abundance (Figure 3B). Moreover, in comparison to all other CD8<sup>+</sup> T cells present in the animals at day 5, these cells clearly expressed elevated levels of both glycolytic and oxidative proteins (Figures 3C and S3A). Therefore, early activated T cells exhibited peak expression of metabolic mediators of oxidative and glycolytic pathways.

A key advantage of any single-cell approach is the ability to resolve novel insights of cellular behavior and function by

revealing heterogeneity within canonical populations. Therefore, to confirm the co-expression of metabolic proteins across key metabolic pathways within individual early-activated CD8<sup>+</sup> cells, we visualized glycolytic and oxidative markers by scatterplots. This visualization approach clearly demonstrated that early activated CD8<sup>+</sup> T cells co-expressed CPT1a and Glut1 compared to all other CD8<sup>+</sup> T cells at day 5 p.i. Similar co-expression profiles between GAPDH and ATP5a were also noted and confirmed that glycolytic and oxidative proteins are co-expressed at the single-cell level in early-activated T cells. Similar co-expression profiles were noted between HADHA and CD98, demonstrating co-expression of proteins involved in branched-chain amino acid import and long-chain FAO in during this phase of T cell activation (Figure 3D). To further evaluate co-expression of metabolic proteins of interest with single-cell resolution, we took another complementary approach by computing pairwise correlations for each metabolic protein across single early-activated CD8<sup>+</sup> T cells. Consistent with the prior results, all studied metabolic proteins were positively correlated, without evidence of negative correlations between oxidative and glycolytic markers (Figure S3B). Taken together, these results indicated that oxidative and glycolytic proteins were indeed co-expressed in individual early-activated CD8<sup>+</sup> T cells. They also demonstrated the ability to resolve metabolic marker expression at the single-cell level by mass cytometry.

### Early-activated T cells demonstrate peak glycolytic activity and increased mitochondrial activity and mass

Since these early-activated T cells were distinguished by simultaneously elevated levels of glycolytic and oxidative enzymes, we posited that this expression profile would translate to greater metabolic activity along these pathways when compared to their SLEC counterparts. To assess real-time bioenergetic flux through oxidative and glycolytic pathways, we sorted naive, early-activated, and SLEC T cells for analysis by Seahorse assay (Figure S3B). As expected, SLECs demonstrated significantly higher baseline and maximum extracellular acidification rates (ECARs) compared to their naive counterparts (Figure 3D), confirming a predominantly glycolytic program driving the terminal effector state *in vivo*. However, in accordance with their enzymatic expression profile by mass cytometry, early-activated T cells exhibited significantly higher basal and maximal ECARs even compared to SLECs (Figure 3D).

Moreover, baseline and maximal OCRs did not significantly differ between the SLEC and naive pools, as described previously (van der Windt et al., 2012; Figures 3E and 3F). However,

**Figure 3. Early-activated T cells exhibit a distinctive metabolic profile characterized by peak oxidative and glycolytic activity**

- (A) Biaxial scatterplots indicating surface marker expression profile of the early-activated T cell pool.
  - (B) Frequency of early-activated cells during days 0–9 p.i.
  - (C) Metabolic expression profiles of metabolic and signaling markers in early-activated T cells in comparison to all other CD8<sup>+</sup> T cells during days 0–9 p.i. as depicted by histograms. Significance analysis of all medians by paired two-tailed Student's t test is displayed.
  - (D) Scatterplots denoting the expression of proteins involved in glycolysis, long-chain fatty acid oxidation (FAO), oxidative phosphorylation, and branched-chain amino acid metabolism in early-activated CD8<sup>+</sup> T cells on day 5 p.i.
  - (E–G) CD8<sup>+</sup> T cell subsets of interest were sorted on days 5 (naive cells and early-activated cells) and 8 (SLECs) p.i. and analyzed by mitochondrial stress test ( $n = 5$  mice per time point). (E) Basal ECAR and maximal ECAR measured upon oligomycin administration. (F) OCR over time. (G) Basal and maximal OCR readings obtained upon FCCP administration.
  - (H) MitoTracker signal in each subset ( $n = 5$  mice per subset).
- Significance analysis by paired two-tailed Student's t test (\* $p < 0.05$ ; \*\* $p < 0.01$ ). Error bars represent SEM. Data are representative of at least two independent experiments.

early-activated T cells did indeed exhibit significantly higher oxidative activity compared to both SLECs and naive cells (Figures 3E and 3F). Since these cells exhibited maximal expression of electron transport complexes, we hypothesized that this population would possess SRC. Indeed, while neither the naive nor SLEC pool was capable of surpassing the baseline OCR upon FCCP administration, the OCR of early-activated T cells nearly doubled (Figures 3E and 3F).

We next determined whether these cells could utilize exogenous fatty acids as an energy source. Consistent with a prior study (Raud et al., 2018), naive T cells exhibited a higher OCR in the presence of palmitate. In comparison, early-activated cells also exhibited an increase in OCRs in the presence of palmitate to levels that also exceeded those of naive cells, confirming their ability to oxidize fatty acids. As we observed from cells activated *in vitro*, SRC was largely independent of the presence of exogenous palmitate (Figures S3C and S3D). As SRC has been associated with greater mitochondrial mass (Buck et al., 2016), we sought to quantify the mitochondrial content of these cells using MitoTracker Deep Red, a fluorescent dye staining mitochondria in live cells. Consistent with our mass cytometry and Seahorse data, the early-activated T cells contained significantly more mitochondrial mass than the SLEC or naive pools (Figure 3G). Overall, these observations confirmed the unique, simultaneously oxidative, and glycolytic profile of early-activated T cells.

#### Antigen-specific CD8<sup>+</sup> T cells transit through the early-activation state commensurate with the onset of proliferation

In order to query the antigen specificity of these metabolic adaptations of early T cell activation, we adoptively transferred OT-1 T cells pooled from three naive donors into congenic hosts, which were then infected with Lm-OVA. Splenocytes from recipient mice were analyzed daily from days 3 through 7 p.i. for metabolic analysis by mass cytometry (Figures 4A, 4B, and S4A). A reserved aliquot of the initial OT-1 T cells that were transferred was also analyzed in parallel as a baseline sample. Indeed, unsupervised clustering analysis of adoptively transferred OT-1 T cells revealed early-activated cells with an analogous state of metabolic activity, arising in small numbers at day 3 p.i. and peaking at day 4 before rapidly regressing by day 5 (Figures 4A, 4B, and S4A). The kinetics of the emergence of this cluster were slightly earlier compared to the previously characterized endogenous cells, perhaps a result of higher TCR affinity or increased frequency of antigen-specific precursor cells. Consistent with our findings in endogenous CD8<sup>+</sup> T cells (Figures 2C and 3C), cells comprising this cluster exhibited simultaneous peak expression of markers of glycolysis, OXPHOS, and LCFA oxidation (Figures 4C and S4A). We hypothesized that these metabolic adaptations were undertaken in support of clonal expansion of antigen-specific populations. Therefore, we assessed the proliferation of adoptively transferred OT-1 T cells labeled with carboxyfluorescein diacetate succinimidyl ester (CFSE) on days 3–7 p.i. by flow cytometry. Commensurate with the emergence of this early-activated metabolic state, the first antigen-specific T cells to divide did so at day 4 p.i. (Figure 4D). By day 5 p.i., all adoptively transferred cells had divided multiple times (Figure 4D). Consistent with this finding, the total

number of OT1 T cells only modestly increased between days 3 and 4 p.i., but they subsequently rapidly expanded between days 4 and 5 p.i. before plateauing thereafter (Figure 4E). These observations collectively suggested that early-activated antigen-specific CD8<sup>+</sup> T cells underwent a transition to a metabolic state characterized by peak OXPHOS and glycolytic activity at the same time as they began blasting, supporting the dramatic expansion of these cells during productive immune responses.

#### The early-activated state is transient and precedes the development of both effector and memory cells

As early-activated CD8<sup>+</sup> T cells with peak metabolic protein expression were highly transient, only detectable for a few days during the immune response, we investigated the changes that take place in these cells thereafter. We sorted early-activated T cells and transferred them into congenic hosts before isolating splenic T cells 4 days later (Figure 4A). At the end of this period of time, the transferred early-activated cells had given rise to a mixture of cells with phenotypes consistent with SLECs (KLRG1<sup>+</sup>CD127<sup>-</sup>), double-positive cells (KLRG1<sup>+</sup>CD127<sup>+</sup>), and memory cells (KLRG1<sup>-</sup>CD127<sup>+</sup>). Further analysis of the CD127<sup>+</sup> KLRG1<sup>-</sup> memory fraction indicated that most of these cells lack expression of CD62L, consistent with an effector memory phenotype, while a smaller fraction expressed CD62L, consistent with a central memory phenotype (Figure 4B). In addition, we investigated the expression of both CD27 and TCF1 in these subsets, both markers associated with memory cells (Figure 4C). Consistent with our expectations, the memory (CD127<sup>+</sup>KLRG1<sup>-</sup>) and double-positive (CD127<sup>+</sup>KLRG1<sup>+</sup>) cells expressed higher levels of these proteins. We also observed that the memory cells did not express CD69. Given the transient, elevated expression of cell-cycle markers by the early-activated cells (Figure 2C), we hypothesized that these cells would proliferate upon adoptive transfer. Indeed, these cells expanded but lost expression of Ki67 over the course of the 4 days (Figures 5 and S5A). These early-activated T cells also decreased expression of CD25 and ICOS as well as granzyme B by this later time point (Figures 5D and S5B). Consistent with a transient burst of metabolic activity, these cells exhibited markedly lower expression of both glycolytic and oxidative markers at this later time point compared to the early-activated T cells from which they originated (Figures 5D and S5B). Collectively, these data indicated that during CD8<sup>+</sup> T cell differentiation, early-activated T cells underwent a transient period of peak metabolic activity. Thereafter, decreased expression of glycolytic and oxidative pathways took place coordinate with differentiation into short-lived or memory cells.

To better understand the potential of the early-activated T cell pool to generate functional memory responses, we transferred early-activated T cells at day 5 p.i. from CD45.2<sup>+</sup> mice into naive CD45.1<sup>+</sup> congenic recipient mice (Figure 5E). These recipient mice were subsequently infected with Lm-OVA 21 days after the initial infection event. As expected, CD45.2<sup>+</sup> cells were nearly undetectable in unchallenged recipients, consistent with a contracted state (Figure 5F). However, upon challenge with Lm-OVA, CD45.2<sup>+</sup> transferred cells expanded significantly as a percentage of CD8<sup>+</sup> T cells and in absolute numbers, consistent with the re-expansion of a memory population (Figure 5F). As an alternative approach, we also

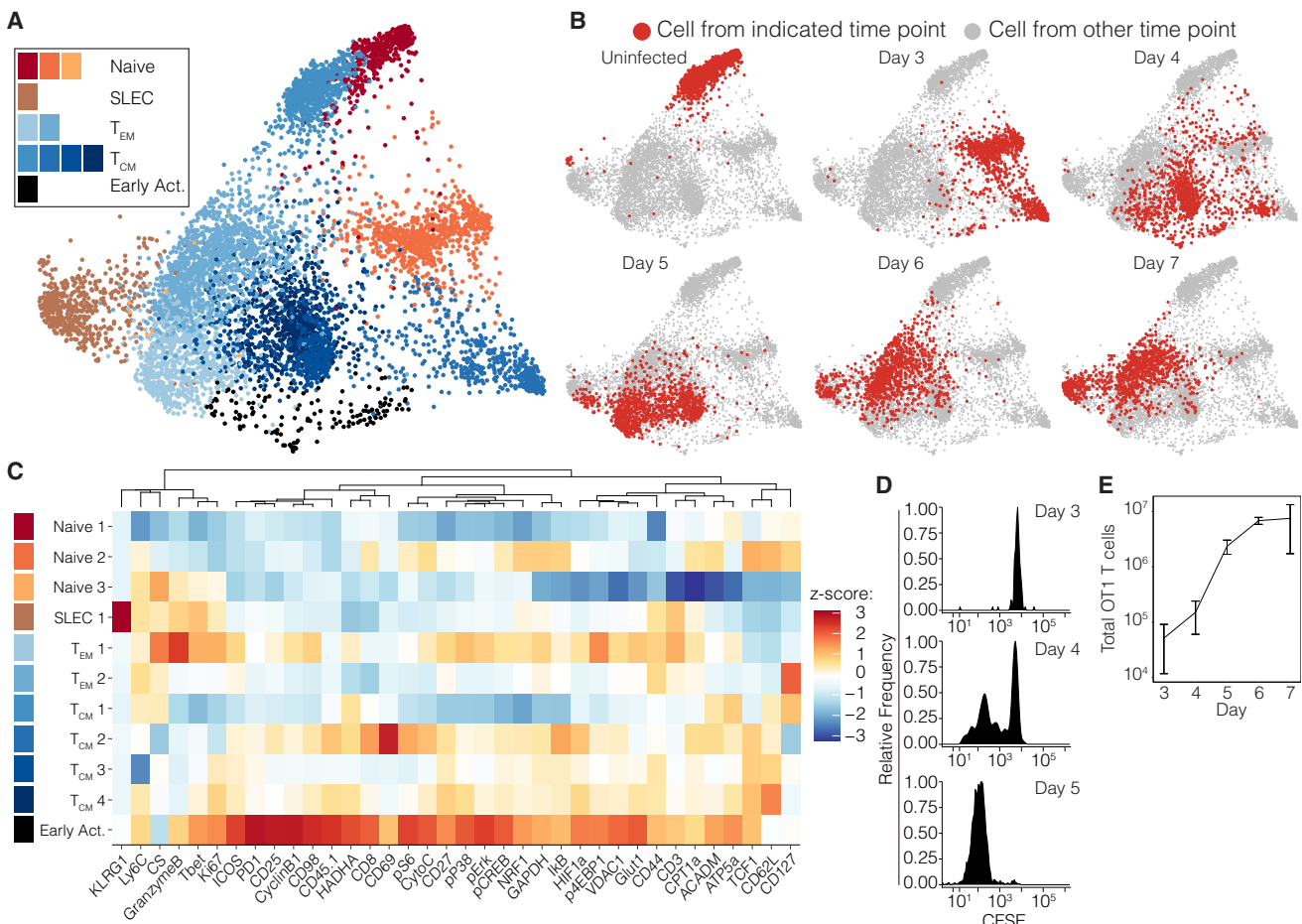


**Figure 4. Antigen-specific CD8<sup>+</sup> T cells transit through the early-activated metabolic state**

OT-1 T cells pooled from three naive mice were adoptively transferred into congenic hosts, which were then infected with  $5 \times 10^4$  colony-forming units (CFUs) Lm-OVA. Splenocytes were harvested daily on days 3–7 p.i. for metabolic analysis by mass cytometry.

(A) Pooled OT1 cells from uninfected mice or after transfer into recipient mice and on days 3–7 after Lm-OVA infection ( $n = 3$  mice per time point except day 3 ( $n = 1$ )) clustered by Phenograph and visualized by a force-directed graph.

(B) Force-directed graphs indicating cellular distribution by time point.

(C) Functional and phenotypic median expression profiles for each CD8<sup>+</sup> T cell cluster.

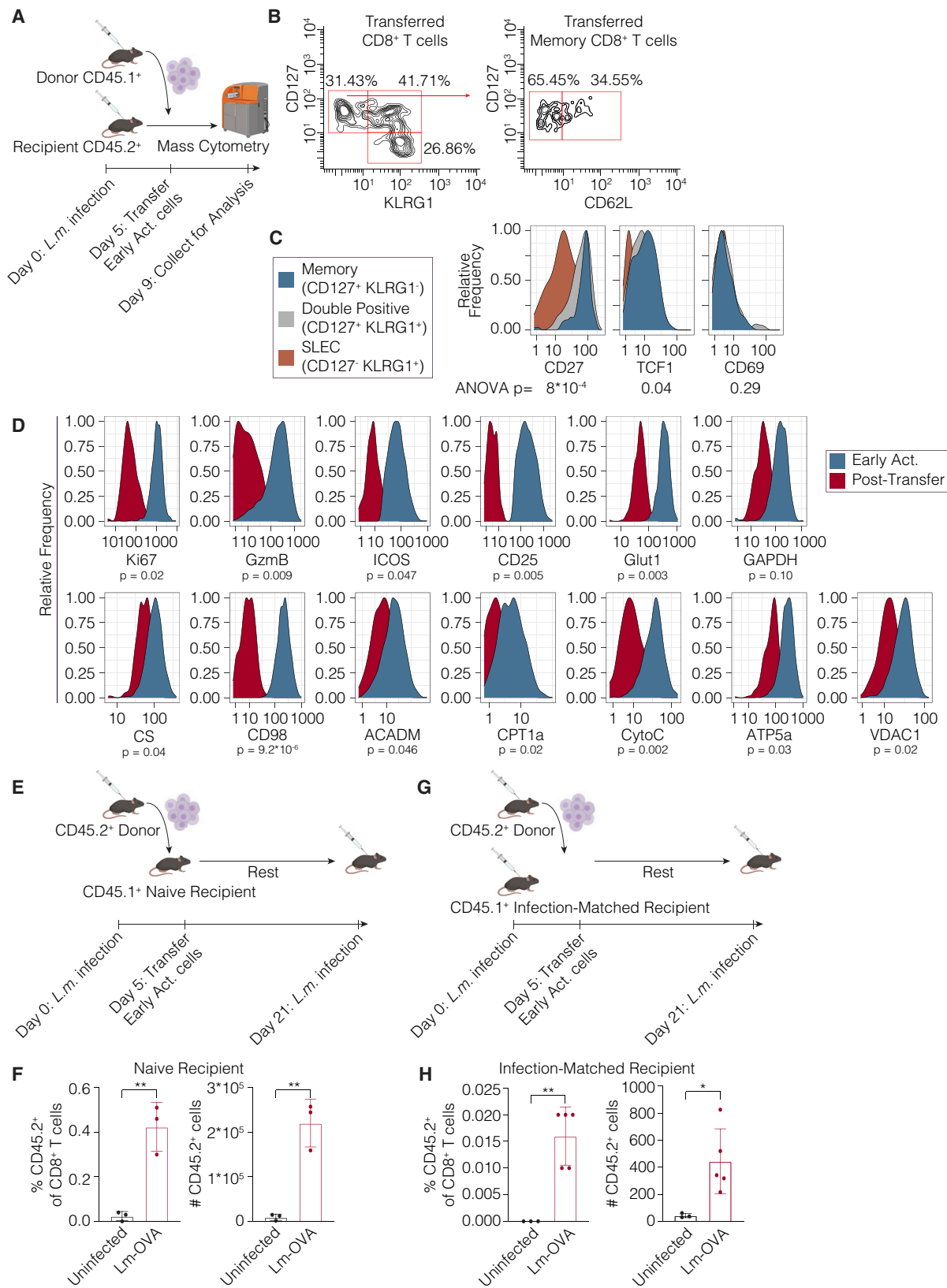
(D and E) Proliferation of adoptively transferred OT1s as measured by CFSE dilution at days 3–5 p.i. (D) and absolute cell counts at days 3–7 p.i. (E).

adoptively transferred CD45.2<sup>+</sup> early-activated T cells at day 5 p.i. into infection-matched CD45.1<sup>+</sup> recipient mice, which were subsequently rechallenged with Lm-OVA 21 days after the initial infection (Figure 5G). CD45.2<sup>+</sup> transferred cells expanded significantly upon rechallenge once again (Figure 5H). Taken together, these data confirmed that early-activated cells can differentiate into memory cells capable of mounting functional recall responses.

#### Single-cell metabolic dynamics of CAR T cells in response to malignancy

A study utilized mass cytometry to assess changes in metabolic protein expression in human immune cells stimulated *in vitro* (Hartmann et al., 2020). Therefore, we extended that approach to understand the metabolic dynamics of antigen-specific T cells over the course of a human immune response *in vivo*. We assessed the metabolic adaptations in chimeric antigen receptor (CAR) T cells over time. Axicabtagene ciloleucel CAR

T cell products were sampled from two patients with advanced refractory diffuse large B-cell lymphoma (DLBCL) at the time of infusion, and peripheral blood mononuclear cells (PBMCs) were also isolated from these same patients on days 7, 14, 21, 28, and 90 after CAR T cell infusion for functional analysis by mass cytometry (Figure 6A; Table S1). Dimensionality reduction revealed that CD8<sup>+</sup> CAR T cells at the time of infusion were distinct from cells at all other time points (Figure 6B). At the time of infusion, adoptively transferred CAR T cells exhibited analogous metabolic dynamics to the early-activated T cells in mice, with peak oxidative and glycolytic marker expression (Figure 6C). Most metabolic proteins were subsequently diminished by day 7 of treatment, with decreasing expression thereafter (Figure 6C). Notably, Spearman correlation analysis demonstrated that there was a positive association between oxidative phosphorylation and glycolytic proteins at the time of infusion, suggesting that these processes are not mutually exclusive (Figure 6D). Moreover, consistent with our mouse models of



(legend on next page)

infection, ICOS was also uniquely expressed by cells in this early-activated state (Figure 6E).

## DISCUSSION

Mass cytometry permits broad-spectrum characterization of immune responses in healthy and diseased states (Spitzer and Nolan, 2016). To date, this approach has been used to query the phenotypic and signaling adaptations undertaken by cells during differentiation (Bendall et al., 2014; Zunder et al., 2015). However, the coordinated downstream metabolic cues supporting these programs *in vivo* have remained incompletely understood at the single-cell level. Here, we directly measured the expression levels of essential nutrient receptors, enzymes, signaling intermediates, and markers of cellular differentiation and effector function at the proteomic level. This allowed us to more thoroughly characterize CD8<sup>+</sup> T cell responses during acute infection, highlighting the metabolic adaptations of canonical T cell subsets and capturing a unique metabolic state in rare, early-activated T cells.

The field of immunometabolism is rapidly advancing, with novel techniques accelerating our capability to resolve metabolism at the single-cell level (Artyomov and Van den Bossche, 2020). Cytometry-based assays have been used to study the metabolic programs of human immune cells *in vitro* (Ahl et al., 2020; Hartmann et al., 2020). Here, we have adapted mass cytometry to study the metabolic trajectories of both murine and human antigen-specific immune responses *in vivo*. Moreover, we have leveraged these tools to probe context-dependent metabolic heterogeneity, identifying and validating transitional metabolic states arising during CD8<sup>+</sup> T cell differentiation. We propose that this discovery-driven approach may be used by investigators to identify and understand metabolic states of various cell types *in vivo* across a wide range of contexts.

Previous models based on bulk data have proposed a reliance of effector T cells on aerobic glycolysis (Sukumar et al., 2013; Wang et al., 2011). However, a prior study of intracellular flux in activated T cells has reported that effector T cells may utilize oxidative phosphorylation *in vivo* (Ma et al., 2019). Additionally, it has been observed that effector T cells engage in more active LCFA uptake than their memory cell counterparts, which instead have been shown to mobilize these substrates from lysosomal triglycerides (O'Sullivan et al., 2014). It is therefore feasible that fatty acid uptake may provide additional substrate for OXPHOS early in the course of T cell activation. Our data unify these obser-

vations, supporting a coordinated program in which glycolysis and OXPHOS are maintained simultaneously in individual cells during an earlier stage of T cell activation.

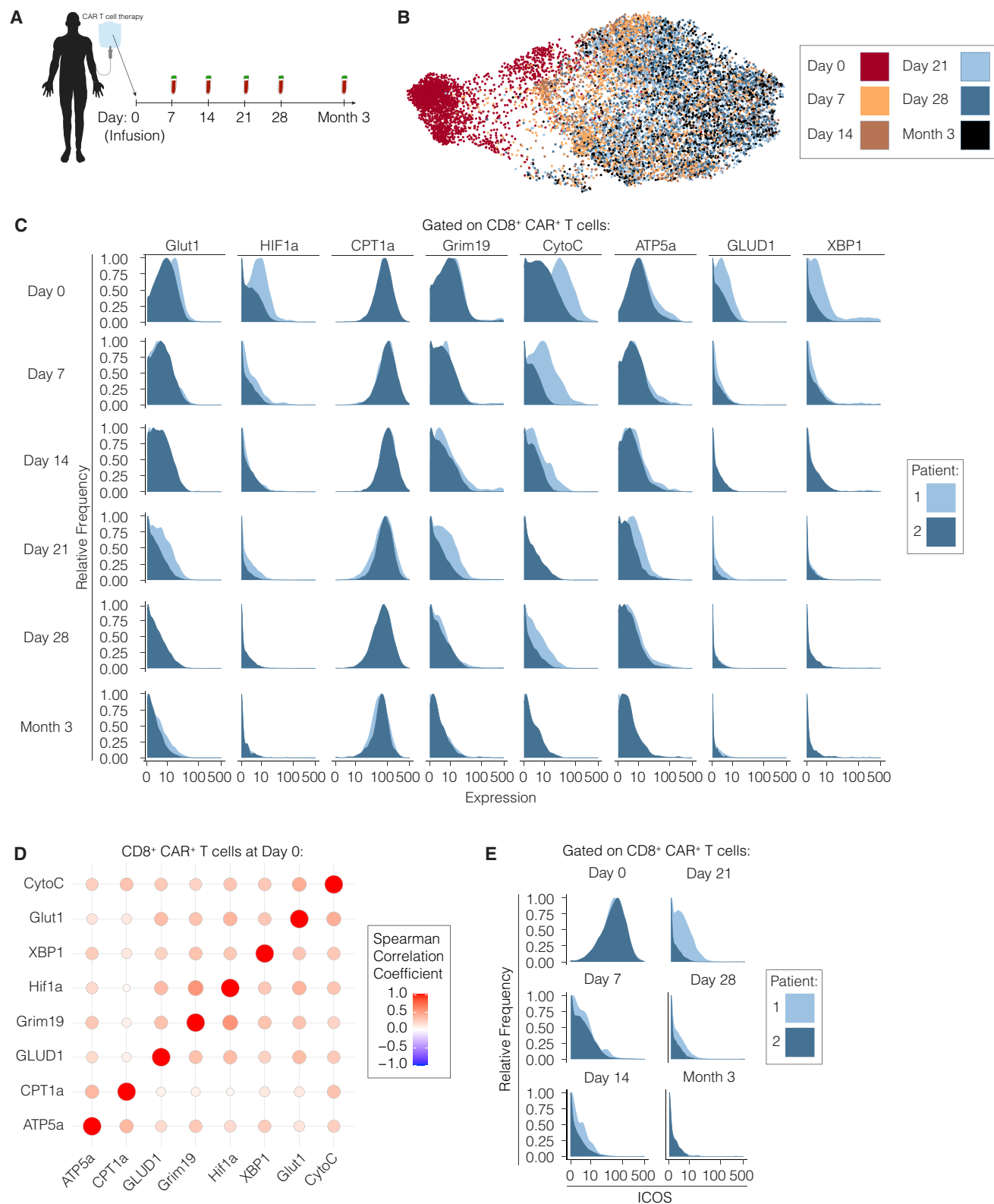
Our approach to metabolic profiling by mass cytometry affords investigators the opportunity to functionally characterize the metabolic adaptations of rare cellular populations, such as antigen-specific T cells. These cells would be otherwise difficult to analyze by current standard metabolomics assays due to the prohibitively large number of cells, extensive processing, and *ex vivo* culture techniques required for these studies (Cantor et al., 2017; van der Windt et al., 2016). Here, we were able to characterize the metabolic, signaling, and phenotypic progeny of adoptively transferred cells with single-cell resolution. This approach revealed a diversification during CD8<sup>+</sup> T cell differentiation in the context of acute infection, with a highly metabolically active and proliferative state in T cells early in the course of their response, which later decrease expression of specific metabolic pathways as they differentiate into both memory and terminal effector cells.

The maximal expression of metabolic proteins early after T cell activation suggests a potential role for TCR ligation and/or co-stimulation during CD8<sup>+</sup> T cell priming. Notably, 4-1BB ligation during co-stimulation has been shown to induce mitochondrial fusion via TRAF2-mediated signaling through p38 and PGC1α (Menk et al., 2018a; Teijeira et al., 2018). Similarly, CD28 ligation has been demonstrated to induce CPT1a expression *in vitro* (Klein Geltink et al., 2017). Whether these signals potentiate the observed SRC and increased mitochondrial mass in early-activated T cells will be important to determine. As Drp1-mediated mitochondrial fission has been described in effector cells during metabolic reprogramming to the aerobic glycolytic program (Buck et al., 2016), it is possible that the absence of co-stimulation and loss of IL-2 signaling upon pathogen clearance may result in mitophagy and/or mitochondrial fission, repressing oxidative activity in terminal effector subsets.

As the importance of metabolism to immune cell fate and function is increasingly appreciated, methods to evaluate these pathways in models of productive and dysregulated immune responses will be critical. The approach presented here may be adapted to any cell type of interest, including both immune cells and non-immune cells, such as interacting epithelial tissues or tumors. This methodology should enable investigators to study the functional programs underlying the development of the full spectrum of immune cell lineages and their altered states in the context of autoimmunity or malignancy. Additionally, integrated functional analysis of rare cellular subsets will permit

**Figure 5. The early-activated state is transient and differentiates into effector and memory cells**

- (A) Early-activated T cells were sorted from CD45.1<sup>+</sup> mice on day 5 p.i. and transferred into infected CD45.2<sup>+</sup> hosts on day 5 p.i (n = 2 per group) before sacrifice 4 days later for analysis by mass cytometry.
  - (B) Differentiation state of early-activated cells determined by CD44 and KLRG1 expression at day 9 p.i.
  - (C) Histograms of memory markers expressed by adoptively transferred early-activated T cells at day 9 p.i.
  - (D) Metabolic and signaling marker profiles before and after transfer at days 5 and 9 p.i. are represented by histograms.
  - (E) Early-activated T cells isolated from CD45.2 mice at day 5 p.i. were adoptively transferred into naive CD45.1<sup>+</sup> recipient mice. Recipient animals were either infected with  $1.0 \times 10^5$  CFUs Lm-OVA or left unchallenged (n = 3 mice per group).
  - (F) Percentages and absolute cell counts of CD45.2<sup>+</sup> CD8<sup>+</sup> T cells in uninfected and challenged recipients.
  - (G) Early-activated T cells isolated from CD45.2 mice at day 5 p.i. were adoptively transferred into infection-matched CD45.1<sup>+</sup> recipient mice. Recipient animals were either infected with  $1.0 \times 10^6$  CFUs Lm-OVA or left unchallenged (n = 3–5 mice per group).
  - (H) Percentages and absolute cell counts of CD45.2<sup>+</sup> CD8<sup>+</sup> T cells in uninfected and rechallenged recipients.
- Significance analysis by unpaired Student's t test (\*p < 0.05; \*\*p < 0.005).



(legend on next page)

simultaneous evaluation of the effects of various treatments on rare populations, such as tumor-infiltrating lymphocytes or neo-antigen-specific T cells.

### Limitations of study

While our approach enables single-cell characterization of cellular metabolism, limitations of the current study afford opportunities to further validate and build on this work. While we elected to pursue an integrated analysis of signaling, metabolism, and effector function, a more refined survey of additional enzymes along specific pathways, with particular emphasis on anabolic processes, would provide additional insights into the mechanisms governing T cell activation and differentiation. Moreover, direct measurement of epigenetic regulators of these metabolic processes by either mass cytometry or ATAC-seq would further facilitate understanding of the concerted processes underlying the transition to the early-activated state reported in our study. As metabolic state is driven by substrate availability in addition to cellular adaptations, additional orthogonal methods such as metabolic flux analysis will continue to determine the relative contributions of pathways of interest.

### STAR★METHODS

Detailed methods are provided in the online version of this paper and include the following:

- [KEY RESOURCES TABLE](#)
- [RESOURCE AVAILABILITY](#)
  - Lead contact
  - Materials availability
  - Data and code availability
- [EXPERIMENTAL MODEL AND SUBJECT DETAILS](#)
  - Animals
  - Human subjects
  - Infectious agents
- [METHOD DETAILS](#)
  - Mass cytometry antibodies
  - *In vitro* OT1 stimulation and polarization
  - Cell preparation
  - Mass-tag cellular barcoding
  - Mass cytometry staining and measurement
  - Mass cytometry bead standard data normalization
  - Adoptive T cell transfer
  - Flow cytometry and cell sorting
  - Extracellular flux analysis
- [QUANTIFICATION AND STATISTICAL ANALYSIS](#)
  - Statistical analysis
  - Unsupervised clustering analysis
  - Data visualization

### SUPPLEMENTAL INFORMATION

Supplemental Information can be found online at <https://doi.org/10.1016/j.immuni.2021.02.018>.

### ACKNOWLEDGMENTS

We would like to thank the members of the Spitzer lab, Vinh Ngyuen, Stanley Tamaki, Sagar Bapat, Adil Daud, Lawrence Fong, Andrei Goga, and Rushika Perera for their experimental contributions and helpful discussions. *Listeria monocytogenes* strain 10403s expressing OVA (Lm-OVA) was kindly provided by Shomyseh Sanjabi (UCSF). We acknowledge the Parnassus Flow Cytometry Core Facility, which is supported in part by NIH grants P30DK063720, S10OD018040, S10OD018040, and S10OD021822. Recombinant human IL-2 (IL-2, TECIN, Teceleukin) was provided by the National Cancer Institute. This work was supported by NIH grant DP5OD023056 to M.H.S. and grants R01DK105550 and R01HL136664 to J.C.R. M.Z.M was supported by NIH grant F30CA239367. L.S.L. was supported by Conquer Cancer Foundation Young Investigator Award grant CA-0122026. M.H.S. is a Chan Zuckerberg Biohub investigator and a Parker Institute for Cancer Immunotherapy investigator.

### AUTHOR CONTRIBUTIONS

L.S.L., K.J.H.-G., M.Z.M., O.O.O., J.M.I., J.C.R., and M.H.S. conceptualized this study and designed experiments. L.S.L., K.J.H.-G., D.M.M., I.T., M.Z.M., D.C.C., and D.O.D. performed experiments. L.S.L., K.J.H.-G., M.Z.M., and M.H.S. performed data analysis. L.S.L. and M.H.S. wrote the manuscript. M.H.S. supervised the study.

### DECLARATION OF INTERESTS

O.O.O. received honoraria from Kite Pharmaceuticals; consultant fees from Kite, Pfizer, Spectrum, Curio Science, and Bayer; and research funding from Kite. J.C.R. is founder and member of the scientific advisory board of Sitryx Therapeutics; is a member of the scientific advisory boards of Caribou Biosciences and Istesso; and received research funding from Kadmon, Incyte, Tempest, and Calithera and honoraria from Merck and Pfizer. M.H.S. is founder and a board member of Teiko Bio; received consultant fees from Five Prime Therapeutics, Earli, Ono Pharmaceutical, and January; and received research funding from Roche/Genentech, Pfizer, Valitor, and Bristol-Myers Squibb.

Received: June 9, 2020

Revised: December 8, 2020

Accepted: February 17, 2021

Published: March 10, 2021

### REFERENCES

- Ahl, P.J., Hopkins, R.A., Xiang, W.W., Au, B., Kaliaperumal, N., Fairhurst, A.-M., and Connolly, J.E. (2020). Met-Flow, a strategy for single-cell metabolic analysis highlights dynamic changes in immune subpopulations. *Commun. Biol.* 3, 305.
- Ahmed, R., and Gray, D. (1996). Immunological Memory and Protective Immunity: Understanding Their Relation. *Science* 272, 54–60.
- Andrejeva, G., and Rathmell, J.C. (2017). Similarities and Distinctions of Cancer and Immune Metabolism in Inflammation and Tumors. *Cell Metab.* 26, 49–70.

**Figure 6. CAR T cells exhibit an analogous transient early-activated program upon infusion into advanced non-Hodgkin lymphoma patients**  
 (A) Axicabtagene ciloleucel CAR T cells from two advanced non-Hodgkin lymphoma patients were sampled at the time of infusion, and PBMCs were isolated from the same patients on days 7, 14, 21, and 28 and month 3 post-infusion for analysis by mass cytometry.  
 (B) Pooled CD8<sup>+</sup> CAR T cells from all time points post-infusion visualized by a force-directed graph.  
 (C) Expression levels of key metabolic markers by CAR T cells at each time point post-infusion by patient.  
 (D) Spearman correlation matrix of CAR T cells at time of infusion (day 0) into advanced lymphoma patients.  
 (E) ICOS expression in individual patients at each time point post-infusion represented by histograms.

- Araki, K., Turner, A.P., Shaffer, V.O., Gangappa, S., Keller, S.A., Bachmann, M.F., Larsen, C.P., and Ahmed, R. (2010). HHS Public Access. 460, 108–112.
- Artymov, M.N., and Van den Bossche, J. (2020). Immunometabolism in the Single-Cell Era. *Cell Metab.* 32, 710–725.
- Badovinac, V.P., Haring, J.S., and Harty, J.T. (2007). Initial T cell receptor transgenic cell precursor frequency dictates critical aspects of the CD8(+) T cell response to infection. *Immunity* 26, 827–841.
- Bandura, D.R., Baranov, V.I., Ornatsky, O.I., Antonov, A., Kinach, R., Lou, X., Pavlov, S., Vorobiev, S., Dick, J.E., and Tanner, S.D. (2009). Mass cytometry: technique for real time single cell multitarget immunoassay based on inductively coupled plasma time-of-flight mass spectrometry. *Anal. Chem.* 81, 6813–6822.
- Bendall, S.C., Simonds, E.F., Qiu, P., Amir, E.A.D., Krutzik, P.O., Finck, R., Bruggner, R.V., Melamed, R., Trejo, A., Ornatsky, O.I., et al. (2011). Single-cell mass cytometry of differential immune and drug responses across a human hematopoietic continuum. *Science* 332, 687–696.
- Bastian, M., Heymann, S., and Jacomy, M. (2009). Gephi: an open source software for exploring and manipulating networks. International AAAI Conference on Weblogs and Social Media.
- Bendall, S.C., Davis, K.L., Amir, A.D., Tadmor, M.D., Simonds, E.F., Chen, T.J., Shenfeld, D.K., Nolan, G.P., and Pe'er, D. (2014). Single-cell trajectory detection uncovers progression and regulatory coordination in human B cell development. *Cell* 157, 714–725.
- Bodenmiller, B., Zunder, E.R., Finck, R., Chen, T.J., Savig, E.S., Bruggner, R.V., Simonds, E.F., Bendall, S.C., Sachs, K., Krutzik, P.O., and Nolan, G.P. (2012). Multiplexed mass cytometry profiling of cellular states perturbed by small-molecule regulators. *Nat. Biotechnol.* 30, 858–867.
- Borges da Silva, H., Beura, L.K., Wang, H., Hanse, E.A., Gore, R., Scott, M.C., Walsh, D.A., Block, K.E., Fonseca, R., Yan, Y., et al. (2018). The purinergic receptor P2RX7 directs metabolic fitness of long-lived memory CD8<sup>+</sup> T cells. *Nature* 559, 264–268.
- Buck, M.D., Sowell, R.T., Kaech, S.M., and Pearce, E.L. (2017). Metabolic Instruction of Immunity. *Cell* 169, 570–586.
- Buck, M.D.D., O'Sullivan, D., Klein Geltink, R.I.I., Curtis, J.D.D., Chang, C.H., Sanin, D.E.E., Qiu, J., Kretz, O., Braas, D., van der Windt, G.J.J.W., et al. (2016). Mitochondrial Dynamics Controls T Cell Fate through Metabolic Programming. *Cell* 166, 63–76.
- Callahan, M.K., Postow, M.A., and Wolchok, J.D. (2016). Targeting T Cell Co-receptors for Cancer Therapy. *Immunity* 44, 1069–1078.
- Cantor, J.R., Abu-Remaileh, M., Kanarek, N., Freinkman, E., Gao, X., Louisaint, A., Jr., Lewis, C.A., and Sabatini, D.M. (2017). Physiologic Medium Rewires Cellular Metabolism and Reveals Uric Acid as an Endogenous Inhibitor of UMP Synthase. *Cell* 169, 258–272.e17.
- Carpenter, K., Pollitt, R.J., and Middleton, B. (1992). Human liver long-chain 3-hydroxyacyl-coenzyme A dehydrogenase is a multifunctional membrane-bound beta-oxidation enzyme of mitochondria. *Biochem. Biophys. Res. Commun.* 183, 443–448.
- Carrio, R., Bathe, O.F., and Malek, T.R. (2004). Initial antigen encounter programs CD8<sup>+</sup> T cells competent to develop into memory cells that are activated in an antigen-free, IL-7- and IL-15-rich environment. *J. Immunol.* 172, 7315–7323.
- Cheung, P., Vallania, F., Warsinske, H.C., Donato, M., Schaffert, S., Chang, S.E., Dvorak, M., Dekker, C.L., Davis, M.M., Utz, P.J., et al. (2018). Single-Cell Chromatin Modification Profiling Reveals Increased Epigenetic Variations with Aging. *Cell* 173, 1385–1397.e14.
- Chisolm, D.A., Savic, D., Moore, A.J., Ballesteros-Tato, A., León, B., Crossman, D.K., Murre, C., Myers, R.M., and Weinmann, A.S. (2017). CCCTC-Binding Factor Translates Interleukin 2- and  $\alpha$ -Ketoglutarate-Sensitive Metabolic Changes in T Cells into Context-Dependent Gene Programs. *Immunity* 47, 251–267.e7.
- Chu, T., Tyznik, A.J., Roepke, S., Berkley, A.M., Woodward-Davis, A., Pattacini, L., Bevan, M.J., Zehn, D., and Prlic, M. (2013). Bystander-Activated Memory CD8 T Cells Control Early Pathogen Load in an Innate-like, NKG2D-Dependent Manner. *Cell Rep* 3, 701–708.
- Cunningham, C.A., Hoppins, S., and Fink, P.J. (2018). Cutting Edge: Glycolytic Metabolism and Mitochondrial Metabolism Are Uncoupled in Antigen-Activated CD8<sup>+</sup> Recent Thymic Emigrants. *J. Immunol.* 201, 1627–1632.
- D'Souza, A.D., Parikh, N., Kaech, S.M., and Shadel, G.S. (2007). Convergence of multiple signaling pathways is required to coordinately up-regulate mtDNA and mitochondrial biogenesis during T cell activation. *Mitochondrion* 7, 374–385.
- Dennis, M.K., Field, A.S., Burai, R., Ramesh, C., Whitney, K., Bologa, C.G., Oprea, T.I., Yamaguchi, Y., Hayashi, S., Sklar, L., et al. (2012). Postranscriptional control of T cell effector function by aerobic glycolysis. *Cell* 127, 358–366.
- Feske, S. (2007). Calcium signalling in lymphocyte activation and disease. *Nat. Rev. Immunol.* 7, 690–702.
- Finck, R., Simonds, E.F., Jager, A., Krishnaswamy, S., Sachs, K., Fantl, W., Pe'er, D., Nolan, G.P., and Bendall, S.C. (2013). Normalization of mass cytometry data with bead standards. *Cytometry A* 83, 483–494.
- Fracchia, K.M., Pai, C.Y., and Walsh, C.M. (2013). Modulation of T Cell Metabolism and Function through Calcium Signaling. *Front. Immunol.* 4, 324.
- Gerriets, V.A., and Rathmell, J.C. (2012). Metabolic pathways in T cell fate and function. *Trends Immunol.* 33, 168–173.
- Good, Z., Borges, L., Vivanco Gonzalez, N., Sahaf, B., Samusik, N., Tibshirani, R., Nolan, G.P., and Bendall, S.C. (2019). Proliferation tracing with single-cell mass cytometry optimizes generation of stem cell memory-like T cells. *Nat. Biotechnol.* 37, 259–266.
- Gray, S.M., Amezquita, R.A., Guan, T., Kleinstein, S.H., and Kaech, S.M. (2017). Polycomb Repressive Complex 2-Mediated Chromatin Repression Guides Effector CD8<sup>+</sup> T Cell Terminal Differentiation and Loss of Multipotency. *Immunity* 46, 596–608.
- Hartmann, F.J., Mrdjen, D., McCaffrey, E., Glass, D.R., Greenwald, N.F., Bharadwaj, A., Khair, Z., Verberk, S.G., Baranski, A., Baskar, R., et al. (2020). Single-cell metabolic profiling of human cytotoxic T cells. *Nat. Biotechnol.*
- Harty, J.T., and Badovinac, V.P. (2002). Influence of effector molecules on the CD8(+) T cell response to infection. *Curr. Opin. Immunol.* 14, 360–365.
- Hayashi, K., Jutabha, P., Endou, H., Sagara, H., and Anzai, N. (2013). LAT1 Is a Critical Transporter of Essential Amino Acids for Immune Reactions in Activated Human T Cells. *J. Immunol.* 191, 4080–4085.
- Howie, D., Ten Bokum, A., Necula, A.S., Cobbolt, S.P., and Waldmann, H. (2018). The Role of Lipid Metabolism in T Lymphocyte Differentiation and Survival. *Front. Immunol.* 8, 1949.
- Jiang, J., Lau, L.L., and Shen, H. (2003). Selective depletion of nonspecific T cells during the early stage of immune responses to infection. *J. Immunol.* 171, 4352–4358.
- Joshi, N.S., Cui, W., Chandele, A., Lee, H.K., Urso, D.R., Hagman, J., Gapin, L., and Kaech, S.M. (2007). Inflammation directs memory precursor and short-lived effector CD8(+) T cell fates via the graded expression of T-bet transcription factor. *Immunity* 27, 281–295.
- Kaech, S.M., and Ahmed, R. (2001). Memory CD8<sup>+</sup> T cell differentiation: initial antigen encounter triggers a developmental program in naïve cells. *Nat. Immunol.* 2, 415–422.
- Kalia, V., Sarkar, S., Subramaniam, S., Haining, W.N., Smith, K.A., and Ahmed, R. (2010). Prolonged interleukin-2Ralpha expression on virus-specific CD8<sup>+</sup> T cells favors terminal-effector differentiation *in vivo*. *Immunity* 32, 91–103.
- Klein Geltink, R.I.I., O'Sullivan, D., Corrado, M., Bremser, A., Buck, M.D., Buescher, J.M., Firat, E., Zhu, X., Niedermann, G., Caputa, G., et al. (2017). Mitochondrial Priming by CD28. *Cell* 171, 385–397.e11.
- Krishnaswamy, S., Spitzer, M.H., Mingueneau, M., Bendall, S.C., Litvin, O., Stone, E., Pe'er, D., and Nolan, G.P. (2014). Conditional density-based analysis of T cell signaling in single-cell data. *Science* 346, 1250689–1250689.
- Laforge, M., Rodrigues, V., Silvestre, R., Gautier, C., Weil, R., Corti, O., and Estaquier, J. (2016). NF- $\kappa$ B pathway controls mitochondrial dynamics. *Cell Death Differ.* 23, 89–98.

- Lee, J., Walsh, M.C., Hoehn, K.L., James, D.E., Wherry, E.J., and Choi, Y. (2014). Regulator of fatty acid metabolism, acetyl coenzyme a carboxylase 1, controls T cell immunity. *J. Immunol.* 192, 3190–3199.
- Levine, J.H., Simonds, E.F., Bendall, S.C., Davis, K.L., Amir, E.D., Tadmor, M.D., Litvin, O., Fienberg, H.G., Jager, A., Zunder, E.R., et al. (2015). Data-Driven Phenotypic Dissection of AML Reveals Progenitor-like Cells that Correlate with Prognosis. *Cell* 162, 184–197.
- Ma, E.H., Verway, M.J., Johnson, R.M., Roy, D.G., Steadman, M., Hayes, S., Williams, K.S., Sheldon, R.D., Samborska, B., Kosinski, P.A., et al. (2019). Metabolic Profiling Using Stable Isotope Tracing Reveals Distinct Patterns of Glucose Utilization by Physiologically Activated CD8<sup>+</sup> T Cells. *Immunity* 51, 856–870.e5.
- MacIver, N.J., Blagih, J., Saucillo, D.C., Tonelli, L., Griss, T., Rathmell, J.C., and Jones, R.G. (2011). The liver kinase B1 is a central regulator of T cell development, activation, and metabolism. *J. Immunol.* 187, 4187–4198.
- McGregor, D.D., Koster, F.T., and Mackaness, G.B. (1970). The short lived small lymphocyte as a mediator of cellular immunity. *Nature* 228, 855–856.
- Menk, A.V., Schärping, N.E., Rivadeneira, D.B., Calderon, M.J., Watson, M.J., Dunstane, D., Watkins, S.C., and Delgoffe, G.M. (2018a). 4-1BB costimulation induces T cell mitochondrial function and biogenesis enabling cancer immunotherapeutic responses. *J. Exp. Med.* 215, 1091–1100.
- Menk, A.V., Schärping, N.E., Moreci, R.S., Zeng, X., Guy, C., Salvatore, S., Bae, H., Xie, J., Young, H.A., Wendell, S.G., and Delgoffe, G.M. (2018b). Early TCR Signaling Induces Rapid Aerobic Glycolysis Enabling Distinct Acute T Cell Effector Functions. *Cell Rep.* 22, 1509–1521.
- Mingueneau, M., Krishnaswamy, S., Spitzer, M.H., Bendall, S.C., Stone, E.L., Hedrick, S.M., Pe'er, D., Mathis, D., Nolan, G.P., and Benoist, C. (2014). Single-cell mass cytometry of TCR signaling: amplification of small initial differences results in low ERK activation in NOD mice. *Proc. Natl. Acad. Sci. USA* 111, 16466–16471.
- Nii, T., Segawa, H., Taketani, Y., Tani, Y., Ohkido, M., Kishida, S., Ito, M., Endou, H., Kanai, Y., Takeda, E., and Miyamoto Ki. (2001). Molecular events involved in up-regulating human Na<sup>+</sup>-independent neutral amino acid transporter LAT1 during T-cell activation. *Biochem. J.* 358, 693–704.
- O'Sullivan, D., van der Windt, G.J., Huang, S.C., Curtis, J.D., Chang, C.H., Buck, M.D., Qiu, J., Smith, A.M., Lam, W.Y., DiPlato, L.M., et al. (2014). Memory CD8<sup>(+)</sup> T cells use cell-intrinsic lipolysis to support the metabolic programming necessary for development. *Immunity* 41, 75–88.
- Obar, J.J., and Lefrançois, L. (2010). Early signals during CD8 T cell priming regulate the generation of central memory cells. *J. Immunol.* 185, 263–272.
- Olenchock, B.A., Rathmell, J.C., and Vander Heiden, M.G. (2017). Biochemical Underpinnings of Immune Cell Metabolic Phenotypes. *Immunity* 46, 703–713.
- Pearce, E.L., Walsh, M.C., Cejas, P.J., Harms, G.M., Shen, H., Wang, L.S., Jones, R.G., and Choi, Y. (2009). Enhancing CD8 T-cell memory by modulating fatty acid metabolism. *Nature* 460, 103–107.
- Pollizzi, K.N., Patel, C.H., Sun, I.-H., Oh, M.-H., Waickman, A.T., Wen, J., Delgoffe, G.M., and Powell, J.D. (2015). mTORC1 and mTORC2 selectively regulate CD8<sup>+</sup> T cell differentiation. *J. Clin. Invest.* 125, 2090–2108.
- Raud, B., Roy, D.G., Divakaruni, A.S., Tarasenko, T.N., Franke, R., Ma, E.H., Samborska, B., Hsieh, W.Y., Wong, A.H., Stüve, P., et al. (2018). Etomoxir Actions on Regulatory and Memory T Cells Are Independent of Cpt1α-Mediated Fatty Acid Oxidation. *Cell Metab.* 28, 504–515.e7.
- Ren, W., Liu, G., Yin, J., Tan, B., Wu, G., Bazer, F.W., Peng, Y., and Yin, Y. (2017). Amino-acid transporters in T-cell activation and differentiation. *Cell Death Dis.* 8, 1–9.
- Restifo, N.P., Dudley, M.E., and Rosenberg, S.A. (2012). Adoptive immunotherapy for cancer: harnessing the T cell response. *Nat. Rev. Immunol.* 12, 269–281.
- Rolf, J., Zarrouk, M., Finlay, D.K., Foretz, M., Viollet, B., and Cantrell, D.A. (2013). AMPK $\alpha$ 1: a glucose sensor that controls CD8 T-cell memory. *Eur. J. Immunol.* 43, 889–896.
- Schärping, N.E., Menk, A.V., Moreci, R.S., Whetstone, R.D., Dadey, R.E., Watkins, S.C., Ferris, R.L., and Delgoffe, G.M. (2016). The Tumor Microenvironment Represses T Cell Mitochondrial Biogenesis to Drive Intratumoral T Cell Metabolic Insufficiency and Dysfunction. *Immunity* 45, 374–388.
- Shen, H., Miller, J.F., Fan, X., Kolwyck, D., Ahmed, R., and Harty, J.T. (1998). Compartmentalization of bacterial antigens: differential effects on priming of CD8 T cells and protective immunity. *Cell* 92, 535–545.
- Sinclair, L.V., Rolf, J., Embleton, E., Shi, Y.-B., Taylor, P.M., and Cantrell, D.A. (2013). Control of amino-acid transport by antigen receptors coordinates the metabolic reprogramming essential for T cell differentiation. *Nat. Immunol.* 14, 500–508.
- Spitzer, M.H., Carmi, Y., Reticker-Flynn, N.E., Kwek, S.S., Madhireddy, D., Martins, M.M., Gherardini, P.F., Prestwood, T.R., Chabon, J., Bendall, S.C., et al. (2017). Systemic Immunity Is Required for Effective Cancer Immunotherapy. *Cell* 168, 487–502.
- Spitzer, M.H., Gherardini, P.F., Fragiadakis, G.K., Bhattacharya, N., Yuan, R.T., Hotson, A.N., Finck, R., Carmi, Y., Zunder, E.R., Fantl, W.J., et al. (2015). An interactive reference framework for modeling a dynamic immune system. *Science* 349.
- Spitzer, M.H., and Nolan, G.P. (2016). Mass Cytometry: Single Cells, Many Features. *Cell* 165, 780–791.
- Sukumar, M., Liu, J., Ji, Y., Subramanian, M., Crompton, J.G., Yu, Z., Roychoudhuri, R., Palmer, D.C., Muranski, P., Karoly, E.D., et al. (2013). Inhibiting glycolytic metabolism enhances CD8<sup>+</sup> T cell memory and antitumor function. *J. Clin. Invest.* 123, 4479–4488.
- Tarze, A., Deniaud, A., Le Bras, M., Maillier, E., Molle, D., Larochette, N., Zamzami, N., Jan, G., Kroemer, G., and Brenner, C. (2007). GAPDH, a novel regulator of the pro-apoptotic mitochondrial membrane permeabilization. *Oncogene* 26, 2606–2620.
- Teijeira, A., Labiano, S., Garasa, S., Etxeberria, I., Santamaría, E., Rouzaut, A., Enamorado, M., Azpilikueta, A., Inoges, S., Bolaños, E., et al. (2018). Mitochondrial Morphological and Functional Reprogramming Following CD137 (4-1BB) Costimulation. *Cancer Immunol. Res.* 6, 798–811.
- Vogel, C., and Marcotte, E.M. (2012). Insights into the regulation of protein abundance from proteomic and transcriptomic analyses. *Nat. Rev. Genet.* 13, 227–232.
- Wang, R., Dillon, C.P., Shi, L.Z., Milasta, S., Carter, R., Finkelstein, D., McCormick, L.L., Fitzgerald, P., Chi, H., Munger, J., and Green, D.R. (2011). The transcription factor Myc controls metabolic reprogramming upon T lymphocyte activation. *Immunity* 35, 871–882.
- Wherry, E.J., and Ahmed, R. (2004). Memory CD8 T-cell differentiation during viral infection. *J. Virol.* 78, 5535–5545.
- Wiegand, G., and Remington, S.J. (1986). Citrate synthase: structure, control, and mechanism. *Annu. Rev. Biophys. Biophys. Chem.* 15, 97–117.
- van der Windt, G.J.W., Everts, B., Chang, C.H., Curtis, J.D., Freitas, T.C., Amiel, E., Pearce, E.J., and Pearce, E.L. (2012). Mitochondrial respiratory capacity is a critical regulator of CD8<sup>+</sup> T cell memory development. *Immunity* 36, 68–78.
- van der Windt, G.J.W., Chang, C.-H., and Pearce, E.L. (2016). Measuring Bioenergetics in T Cells Using a Seahorse Extracellular Flux Analyzer. *Curr. Protoc. Immunol.* 113, 3.16B.1–3.16B.14.
- Zeng, H., Cohen, S., Guy, C., Shrestha, S., Neale, G., Brown, S.A., Cloer, C., Kishton, R.J., Gao, X., Youngblood, B., et al. (2016). mTORC1 and mTORC2 Kinase Signaling and Glucose Metabolism Drive Follicular Helper T Cell Differentiation. *Immunity* 45, 540–554.
- Zhang, L., and Romero, P. (2018). Metabolic Control of CD8<sup>+</sup> T Cell Fate Decisions and Antitumor Immunity. *Trends Mol. Med.* 24, 30–48.
- Zunder, E.R., Lujan, E., Goltsev, Y., Wernig, M., and Nolan, G.P. (2015). A continuous molecular roadmap to iPSC reprogramming through progression analysis of single-cell mass cytometry. *Cell Stem Cell* 16, 323–337.

## STAR★METHODS

## KEY RESOURCES TABLE

REAGENT or RESOURCE	SOURCE	IDENTIFIER
<b>Antibodies</b>		
Mass cytometry antibodies are found in Table S1	This paper	N/A
Anti-mouse TCRβ-Brilliant Violet 421 clone H57-59]	BioLegend	Cat#109229; RRID: AB_10933263
Anti-mouse TCRβ-APC clone H57-597	BioLegend	Cat#109211; RRID: AB_313434
Anti-mouse CD8-PE clone 53-6.7	BioLegend	Cat#100708; RRID: AB_312747
Anti-mouse CD8-Brilliant Violet 650 clone 53-6.7	BioLegend	Cat#100741; RRID: AB_11204079
Anti-mouse CD62L- Brilliant Violet 421 clone MEL-14	BioLegend	Cat#104435; RRID: AB_10900082
Anti-mouse CD62L- PE Dazzle clone MEL-14	BioLegend	Cat#104447; RRID: N/A
Anti-mouse KLRG1-PE/Cy7 clone MAFA	BioLegend	Cat#138415; RRID: N/A
Anti-mouse KLRG1- Brilliant Violet 510 clone 2F1/KLRG1	BioLegend	Cat#138421; RRID: N/A
Anti-mouse CD44-PE/Cy7 clone IMJ	BioLegend	Cat#103029; RRID: N/A
Anti-mouse CD44-PercP/Cy5.5 clone IM7	BioLegend	Cat#138418; RRID: N/A
Anti-mouse CD25-FITC clone 3C7	BioLegend	Cat#102006; RRID: AB_961210
Anti-mouse CD25-APC clone 3C7	BioLegend	Cat#101909; RRID: AB_2280288
Anti-mouse CD45.1-PE clone A20	BioLegend	Cat#110708; RRID: AB_313496
Anti-mouse CD45.2-APC clone 104	BioLegend	Cat#109813; RRID: AB_389210
Anti-mouse I-ab-Pacific Blue clone AF6-120.1	BioLegend	Cat#116421; RRID: AB_10613291
Anti-mouse I-ab-PE/Cy7 clone AF6-120.1	BioLegend	Cat#116419; RRID: AB_10575904
Anti-mouse F4/80-APC/Cy7 clone BM8	BioLegend	Cat#123117; RRID: AB_893489
Anti-mouse CD19-APC/Cy7 clone 1D3/CD19	BioLegend	Cat#115529; RRID: N/A
Anti-mouse Ter119-Biotin clone TER119	BioLegend	Cat#116204; RRID: AB_313704
Anti-mouse B220-Biotin clone RA3-6B2	BioLegend	Cat#103204; RRID: AB_312988
Anti-mouse Ly6G-Biotin clone 1A8	BioLegend	Cat#127603; RRID: AB_1186105
Anti-mouse I-ab-Biotin clone AF6-120.1	BioLegend	Cat#116404; RRID: AB_313722
Anti-mouse CD11b-Biotin clone M1/70	BioLegend	Cat# 101204; RRID: AB_312787
Anti-mouse CD11c-Biotin clone N418	BioLegend	Cat# 117303; RRID: AB_313772
Anti-mouse CD4-Biotin clone GK1.5	BioLegend	Cat#100404; RRID: AB_312689
<b>Biological samples</b>		
PMBCs from non-Hodgkin Lymphoma patients	Vanderbilt University Medical Center	<a href="https://vumc.org">https://vumc.org</a>
<b>Chemicals, peptides, and recombinant proteins</b>		
Recombinant Mouse IL-7	Biolegend	Cat# 577802; RRID: N/A
Recombinant human IL-2 (Tecaleukin)	NCI Frederick	Cat# N/A RRID: N/A
MitoTracker Deep Red	Thermo Fisher Scientific	Cat# M22426; RRID: N/A
Zombie UV	BioLegend	Cat# 423108; RRID: N/A
Zombie NIR	BioLegend	Cat# 423105; RRID: N/A
OVA(257-264) SIINFEKL peptide	Invivogen	Cat#vac-sin RRID: N/A
Benzonase	Sigma-Aldrich	Cat# E8263-25KU; RRID: N/A
Cisplatin	Sigma-Aldrich	Cat#P439425MG; RRID: N/A

(Continued on next page)

***Continued***

REAGENT or RESOURCE	SOURCE	IDENTIFIER
Intercalator-Ir	Fluidigm	Cat# 201192B; RRID: N/A
Calibration beads, EQ™ Four Element	Fluidigm	Cat#201078; RRID: N/A
UltraComp eBeads beads	eBioscience	Cat# 01-2222-42; RRID: N/A
Seahorse XF Base RPMI pH 7.4	Agilent Technologies	Part#103576-100; RRID: N/A
TrueStain FcX (anti-mouse CD16/32 antibody (clone 93)	BioLegend	Cat#101320; RRID: N/A
Cell Acquisition Solution	Fluidigm	Cat#201240; RRID: N/A
Glutamine (0.2M), 100X	UCSF Media Production Core Facility	Cat#CCFGB002. RRID: N/A
1M HEPES pH 7.4	UCSF Media Production Core Facility	Cat#CCFGL002. RRID: N/A
Fetal Bovine Serum	Omega	Cat#FB-01 RRID: N/A
GIBCO 2-Mercaptoethanol	Thermo Fisher Scientific	Cat# 21985023 RRID: N/A
XF 100mL Pyruvate Solution	Agilent Technologies	Cat# 103578-100. RRID: N/A
XF 1.0 Glucose Solution	Agilent Technologies	Cat#103577-100. RRID: N/A
XF 200mM Glutamine Solution	Agilent Technologies	Cat#103579-100. RRID: N/A
<b>Critical commercial assays</b>		
MaxPar Antibody Conjugation Kit	Fluidigm	Cat#201300; RRID: N/A
Seahorse XF Palmitate Oxidation Stress Test Kit	Agilent Technologies	Cat#103693-100 RRID: N/A
Seahorse XF Mito Stress Test Kit	Agilent Technologies	Cat#103015-100 RRID: N/A
Seahorse XF Flux Pack	Agilent Technologies	Cat#
EasySep Mouse Streptavidin RapidSpheres Isolation Kit	Stem Cell Technologies	Cat#19860 RRID: N/A
<b>Deposited data</b>		
Mass cytometry data	This paper	
<b>Experimental models: organisms/strains</b>		
Mouse: C57BL/6-Tg(TcraTcrb)1100Mjb/J (OT-1)	Jackson Laboratory	Cat# 003831; RRID: IMSR_JAX:003831
Mouse: B6.SJL-Ptprc <sup>a</sup> Pepc <sup>b</sup> /BoyJ (BoyJ)	Jackson Laboratory	Cat# 002014; RRID: IMSR_JAX002014
Mouse: C57BL/6J	Jackson Laboratory	Cat#000664; RRID: IMSR_JAX000664
Listeria Monocytogenes strain 10403s expressing whome cytoplasmic OVA (Lm-OVA)	Shomyseh Sanjabi (UCSF)	Cat# N/A RRID:N/A
<b>Software and algorithms</b>		
Cytobank analysis software	Cytobank, Inc	<a href="https://cytobank.org">https://cytobank.org</a> RRID: SCR_014043
Cellengine analysis software	Primitybio	<a href="https://primitybio.com/cellengine.html">https://primitybio.com/cellengine.html</a> RRID: N/A
Normalizer	(Finck et al., 2013)	<a href="https://github.com/nolanlab/bead-normalization">https://github.com/nolanlab/bead-normalization</a> , RRID: N/A
RPhenograph	(Levine et al., 2015)	<a href="https://github.com/JinmiaoChenLab/Rphenograph">https://github.com/JinmiaoChenLab/Rphenograph</a> RRID: N/A
Gephi	(Bastian et al., 2009)	<a href="https://gephi.org">https://gephi.org</a> RRID:SCR_004293
Prism v9	GraphPad	<a href="https://graphpad.com/scientific-software/prism/">https://graphpad.com/scientific-software/prism/</a> RRID: SCR_005375
R environment	R Development Core Team	<a href="https://www.r-project.org/">https://www.r-project.org/</a> , RRID:SCR_001905
<b>Other</b>		
Helios mass cytometer	Fluidigm	Cat# N/A
FACSAria II	BD	Cat# NA
LSR II Fortessa	BD	Cat# N/A
XF96 Seahorse Analyzer	Agilent	Cat# N/A

**RESOURCE AVAILABILITY****Lead contact**

Further information and requests for resources and reagents should be directed to and will be fulfilled by the Lead Contact, Matthew Spitzer ([matthew.spitzer@ucsf.edu](mailto:matthew.spitzer@ucsf.edu)).

**Materials availability**

This study did not generate new unique materials. Information regarding antibody conjugates is presented in [Table S1](#).

**Data and code availability**

Mass cytometry data will be made publicly available on Mendeley Data at <https://data.mendeley.com/drafts/cnfkpk2t8m>. No new code or algorithms were developed during this study; however, code will be provided upon request without limitations.

**EXPERIMENTAL MODEL AND SUBJECT DETAILS****Animals**

All mice were housed in an American Association for the Accreditation of Laboratory Animal Care–accredited animal facility and maintained in specific pathogen-free conditions. Animal experiments were approved and conducted in accordance with AN157618. Wild-type female C57BL/6 mice and BoyJ CD45.1 between 8–10 weeks old were purchased from The Jackson Laboratory and housed at our facility. TCR Transgenic OT-I CD45.1 mice and heterozygous CD45.2/CD45.1 mice were bred at our facility. Animals were housed under standard SPF conditions with typical light/dark cycles and standard chow.

**Human subjects**

Samples were collected from two advanced Non-Hodgkin Lymphoma patients receiving Axicabtagene ciloleucel therapy as standard of care. Patient CAR T cell sample collection was approved by the Vanderbilt University Medical Center IRB (#171340).

**Infectious agents**

Listeria monocytogenes strain 10403s expressing whole cytoplasmic OVA (Lm-OVA) was kindly provided by Shomyseh Sanjabi (UCSF). Lm-OVA stocks frozen at –80°C were grown overnight at 37°C in BHI broth supplemented with 5 µg/ml Erythromycin (Bio Basic, Amherst, New York). Then, overnight cultures were sub-cultured by diluting into fresh BHI broth supplemented with 5 µg/ml Erythromycin and grown for 4 hours. Bacteria CFU was then quantified by measuring optical density at 600 nm. For primary infections, bacterial culture was then diluted to 5x10<sup>4</sup> CFU/100 µL in sterile 1X PBS and 100 µL was injected per mouse i.v. via the retroorbital vein. For rechallenge infections, bacteria were diluted to 1x10<sup>5</sup> CFU/100 µL if the host mice were naive or 1x10<sup>6</sup> CFU/100 µL if the host mice were previously infected.

**METHOD DETAILS****Mass cytometry antibodies**

All mass cytometry antibodies and concentrations used for analysis can be found in [Table S1](#). Primary conjugates of mass cytometry antibodies were prepared using the MaxPAR antibody conjugation kit (Fluidigm, South San Francisco, CA) according to the manufacturer's recommended protocol sourcing metals from Fluidigm (Fluidigm, South San Francisco, CA) or Trace Sciences International (Richmond Hill, Canada). Following labeling, antibodies were diluted in Candor PBS Antibody Stabilization solution (Candor Bioscience GmbH, Wangen, Germany) supplemented with 0.02% NaN3 to between 0.1 and 0.3 mg/mL and stored long-term at 4°C. Each antibody clone and lot was titrated to optimal staining concentrations using primary murine samples with all appropriate positive and negative controls: polyclonal murine CD8<sup>+</sup> T cells purified by positive selection kit (Stem Cell Technologies, Vancouver, Canada) stimulated with PMA/Ionomycin via eBioscience Cell Stimulation Cocktail (ThermoFisher Scientific, Waltham, Massachusetts) for 15 minutes, 3 hours and 6 hours or plate-bound CD3 (145-2C11) and soluble CD28 (37.51) antibodies (UCSF Monoclonal Antibody Core, San Francisco) for 3 days, OT-1 splenocytes at day 7 of IL-2 or IL-7 polarization as below, and appropriate CD8<sup>+</sup> T cell subsets (Naive, Short-lived Effector and Central Memory) at Day 8 of Lm-OVA infection. Titration results were cross-referenced to the literature as described in the text.

***In vitro* OT1 stimulation and polarization**

OT-1 polarizations were carried out as previously described (Carrio et al., 2004). Briefly, splenocytes from OT-1 mice were cultured at 1x10<sup>6</sup> cells/mL in 24 well-plates of complete RPMI (UCSF Media Core facility) supplemented with 10% FBS (Omega Scientific, Tarzana, California), 100U/mL penicillin-streptomycin (Fisher Scientific, Hampton, New Hampshire), 2mM L-glutamine (Sigma-Aldrich, St. Louis, Missouri) and 50 µM β-mecaptoethanol (Thermo Fisher Scientific, Waltham, Massachusetts) and 10mM HEPES (UCSF Media Core Facility) in the presence of OVA<sub>257-264</sub> peptide (0.1nM) (Invivogen, San Diego, California) and IL-2 (100U/ml) (Teceleukin) kindly provided by NCI Frederick. After 3 days in culture, activated cells were washed 3 times with RPMI 1640 and recultured in T25 culture flasks at 1x10<sup>5</sup> cells/mL in the presence of either IL-7, IL-15 (Biologics, San Diego, California) or IL-2 (Teceleukin) kindly provided by NCI Frederick. (all cytokines 10ng/ml) After 2 additional days in culture, cells were passaged and recultured under the

same conditions without peptide for an additional two days for total of 7 days in culture. Viability was confirmed by trypan blue exclusion (Thermo Fisher, Waltham, Massachusetts) or mass cytometry as described below.

### Cell preparation

All tissue preparations were performed simultaneously from each individual mouse, as previously reported (Spitzer et al., 2017). After euthanasia by CO<sub>2</sub> inhalation, spleens were collected and homogenized in PBS + 5mM EDTA at 4°C. All tissues were washed with PBS/EDTA and re-suspended 1:1 with PBS/EDTA and 100mM Cisplatin (Enzo Life Sciences, Farmingdale, NY) for 60 s before quenching 1:1 with PBS/EDTA + 0.5% BSA to determine viability as previously described (Spitzer et al., 2015). Cells were centrifuged at 500 g for 5 min at 4°C and re-suspended in PBS/EDTA/BSA at a density between 1-10x10<sup>6</sup> cells/ml. Care was taken to maintain all samples at 4°C during all phases of tissue harvest and preparation except viability staining and fixation. Suspensions were fixed for 10 min at RT using 1.6% PFA (Fisher Scientific, Hampton, New Hampshire) and frozen at -80°C.

For experiments with adoptively transferred OT1 T cells, immunomagnetic enrichment was performed to facilitate the detection of extremely rare cells before proliferation. Following lysis of red blood cells with ACK lysis buffer (ThermoFisher Scientific, Waltham, Massachusetts), EasySep Streptavidin Negative Selection was used with the following biotinylated antibodies: MHCII (AF6-120.1), CD11b (M1/70), Ly6C (RB6-8C5), B220 (RA3-6B2), CD4 (GK1.5), Ter119 (TER-119).

For Seahorse experiments with primary mouse T cell populations, cells were sorted by FACS from splenocytes harvested from naive or *Lm* infected WT C57BL/6 mice. For palmitate Seahorse experiments, CD8<sup>+</sup> T cells were immunomagnetically enriched prior to sorting by EasySep Streptavidin Negative Selection using the following biotinylated antibodies: MHCII (AF6-120.1), CD11b (M1/70), Ly6G (1A8), B220 (RA3-6B2), CD4 (GK1.5), Ter119 (TER-119). Then, viable sorted cells were counted by hemocytometer and Trypan blue staining before proceeding to extracellular flux preparation and analysis.

For experiments with human samples, blood was obtained from two advanced Non-Hodgkin Lymphoma patients receiving axicabtagene ciloleucel therapy as standard of care. Residual CAR T product was rinsed from infusion bags immediately following infusion completion and frozen until analysis. Within two hours of blood collection, patient PBMCs were isolated by centrifugation in CPT tubes (BD, Franklin Lakes, NJ) and frozen at -80°C until analysis.

### Mass-tag cellular barcoding

Mass-tag cellular barcoding was performed as previously described (Zunder et al., 2015). Briefly, 1\*10<sup>6</sup> cells from each animal were barcoded with distinct combinations of stable Pd isotopes in 0.02% saponin in PBS. Samples from any given tissue from each mouse per experiment group were barcoded together. Cells were washed once with cell staining media (PBS with 0.5% BSA and 0.02% NaN3), and once with 1X PBS, and pooled into a single FACS tube (BD Biosciences, San Jose, California). After data collection, each condition was deconvoluted using a single-cell debarcoding algorithm (Zunder et al., 2015).

### Mass cytometry staining and measurement

Cells were resuspended in cell staining media (PBS with 0.5% BSA and 0.02% NaN3), and antibodies against CD16/32 (BioLegend, San Diego, California) were added at 20 mg/ml for 5 min at RT on a shaker to block Fc receptors. Surface marker antibodies were then added, yielding 500 uL final reaction volumes and stained for 30 min at RT on a shaker. Following staining, cells were washed 2 times with cell staining media, then permeabilized with methanol for at 10 min at 4°C. Cells were then washed twice in cell staining media to remove remaining methanol, and stained with intracellular antibodies in 500 uL for 1 hour at RT on a shaker. Cells were washed twice in cell staining media and then stained with 1mL of 1:4000 191/193Ir DNA intercalator (Fluidigm, South San Francisco, CA) diluted in PBS with 4% PFA overnight. Cells were then washed once with cell staining media, once with 1X PBS and once with Cell Acquisition Solution (Fluidigm, South San Francisco, CA). Care was taken to assure buffers preceding analysis were not contaminated with metals in the mass range above 100 Da. Mass cytometry samples were diluted in Cell Acquisition Solution containing bead standards (Fluidigm, South San Francisco, CA) to approximately 10<sup>6</sup> cells per mL and then analyzed on a Helios mass cytometer (Fluidigm, South San Francisco, CA) equilibrated with Cell Acquisition Solution. We analyzed 1-5\*10<sup>5</sup> cells per animal per time point, consistent with generally accepted practices in the field. For adoptive transfer experiments, 1-4\*10<sup>6</sup> cells per animal were analyzed.

PBMCs isolated from advanced non-Hodgkin Lymphoma patients as above were thawed, washed in RPMI media supplemented with 10% FBS, glutamine, HEPES, and beta mercaptoethanol, and rested for 15min in media at 37°C, 5% CO<sub>2</sub>. Cells were counted, and then dispensed into a 96-well plate for staining. Cells were stained in 200nM cisplatin, washed, stained with surface antibodies, washed, fixed with 1.6% PFA, washed, permeabilized in methanol, washed, stained with intracellular antibodies, washed, and resuspended with 191/193Ir DNA intercalator overnight at 4°C as above. Mass cytometry samples were washed, resuspended to 500,000 cells/mL containing bead standards for acquisition on a Helios mass cytometer.

### Mass cytometry bead standard data normalization

Data normalization was performed as previously described (Spitzer et al., 2017). Briefly, just before analysis, the stained and intercalated cell pellet was resuspended in freshly prepared Cell Acquisition Solution containing the bead standard at a concentration ranging between 1 and 2\*10<sup>4</sup> beads/ml. The mixture of beads and cells were filtered through a filter cap FACS tubes (BD Biosciences) before analysis. All mass cytometry files were normalized together using the mass cytometry data normalization algorithm (Finck et al., 2013), which uses the intensity values of a sliding window of these bead standards to correct for instrument fluctuations over time and between samples.

**Adoptive T cell transfer**

For adoptive transfer of early activated (EA) cells and SLECs, T cells were sorted by FACS from splenocytes harvested from WT CD45.2 C57BL/6 mice or CD45.1 BoyJ mice 5 days post-infection. For memory rechallenge experiments, CD8<sup>+</sup> T cells were immunomagnetically enriched prior to sorting by EasySep Streptavidin Negative Selection using the following biotinylated antibodies: MHCII (AF6-120.1), CD11b (M1/70), Ly6G (1A8), B220 (RA3-6B2), CD4 (GK1.5), Ter119 (TER-119). Then, viable sorted cells were counted by hemocytometer and Trypan blue staining, resuspended in sterile PBS and transferred into infection-matched congenic mice intravenously via the retroorbital vein.

For memory rechallenge experiments,  $3 \times 10^5$  EA cells were adoptively transferred into infection matched or naive congenic recipient mice. Recipient mice were then infected 21 days following the primary infection. Recipient mice were then euthanized 5 days post rechallenge for harvesting of spleens and quantification of donor adoptively transferred cells by flow cytometry.

For adoptive transfer of pathogen specific T cells to validate the antigen specificity of the early activated cells, CD8<sup>+</sup> T cells were immunomagnetically enriched from the pooled spleens of three CD45.1<sup>+</sup> OT1 TCR transgenic mice with EasySep Streptavidin Negative Selection using the following biotinylated antibodies: MHCII (AF6-120.1), CD11b (M1/70), CD11c (N418), Gr1 (RB6-8C5), B220 (RA3-6B2), CD4 (GK1.5), Ter119 (TER-119). Viable cells were quantified by counting on a hemocytometer with Trypan blue staining.  $1 \times 10^6$  Cells were then resuspended in sterile PBS and transferred into naive WT CD45.2<sup>+</sup> mice intravenously via the retroorbital vein.

**Flow cytometry and cell sorting**

Cells were stained for viability with Zombie-NIR dye. Cell surface staining was performed in cell staining media (PBS with 0.5% BSA and 0.02% Na3N) for 30 minutes at room temperature. The following anti-mouse antibodies were used: TCR $\beta$  – APC (H57-597), CD8<sup>+</sup> – PE (53-5.8), CD62L – BV421 (MEL-14), KLRG1 – BV510 (2F1/KLRG1), CD44 – PE-Cy7 (IM7), CD25 – FITC (3C7), CD19 – APC-Cy7 (1D3/CD19), F480 APC-Cy7 (BM8). Stained cells were analyzed with an LSR II flow cytometer (BD Biosciences). MitoTracker Deep Red (Thermo Fisher, Waltham, Massachusetts) staining was performed per manufacturer's instructions and as previously ([Scharping et al., 2016](#)). For MitoTracker Deep Red experiments, Zombie-UV dye was used (Biolegend, San Diego, California).

For sorting experiments, cells were prepared as described for flow cytometry and then sorted into FBS containing media (RPMI 1640, 20% FBS, 1% HEPES, 100 mg/mL penicillin/streptomycin) on a FACSaria II (BD Biosciences).

**Extracellular flux analysis**

Seahorse Assays were carried out utilizing Agilent Mitochondrial Stress Test kit as previously ([van der Windt et al., 2012](#)) and per the manufacturer's instructions. For both *in vitro* and *in vivo* experiments,  $2.5 \times 10^5$  cells per well were plated for analysis utilizing Cell-Tak adhesive per manufacturer's instructions. Oxygen consumption rates (OCR) and extracellular acidification rates (ECAR) were measured in XF media (non-buffered RPMI 1640 containing 10 mM glucose, 2mM L-glutamine, and 1 mM sodium pyruvate) under basal conditions and in response to 1  $\mu$ M oligomycin, 1  $\mu$ M fluoro-carbonyl cyanide phenylhydrazone (FCCP) and 100 nM rotenone + 1  $\mu$ M antimycin A (all from Agilent, Santa Clara, California) using a 96 well XF Extracellular Flux Analyzer (EFA) (Agilent, Santa Clara, California).

For palmitate oxidation assays OT-I T cells stimulated with IL-2 and SIINFEKL for 3 days followed by polarization in 10ng/ml IL-7 prior to incubation in FAO media (111 mM NaCl, 4.7mM KCl, 1.25mM CaC12, 2.0mM MgSO4, 1.2mM Na2HPO4, 2.5mM glucose, 0.5mM carnitine, and 5mM HEPES) for 15 minutes with the addition of either palmitate-BSA or BSA for extracellular analysis in the presence of 1.5  $\mu$ M Oligomycin, 1  $\mu$ M FCCP, and 0.5  $\mu$ M Antimycin A/Rotenone as previously ([Raud et al., 2018](#)).

**QUANTIFICATION AND STATISTICAL ANALYSIS****Statistical analysis**

All significance analysis of Seahorse data and cellular frequency was performed by paired two-sided Student's t test with error bars representing SEM in Prism v8. (GraphPad, San Diego, California). Analysis of median protein expression was performed by paired or unpaired (as indicated) two-sided Student's t test in R. Spearman correlation matrices were generated using the Hmisc package in R.

**Unsupervised clustering analysis**

Cell clusters were identified using the Phenograph algorithm as implemented in the 'cytofkit' package in R (Levine et al., 2015). Standard settings were utilized (with k = 30 for endogenous CD8<sup>+</sup> T cells and k = 100 for OT1 T cells).

**Data visualization**

Unsupervised force-directed graphs were generated as previously reported (Spitzer et al., 2015) with the following modifications. Single cells were downsampled to n = 1,000 cells from each time point by randomly selecting cells across the biological replicates. All cells were combined in a single graph with edge weights defined as the cosine similarity between the vectors of marker values of each cell. All the pairwise distances were calculated and for each node only the 10 edges of highest weight were retained. The graph was then laid out using the ForceAtlas2 algorithm in Gephi.

**Supplemental information**

**Single-cell analysis by mass cytometry  
reveals metabolic states of early-activated  
CD8<sup>+</sup> T cells during the primary immune response**

**Lauren S. Levine, Kamir J. Hiam-Galvez, Diana M. Marquez, Iliana Tenvooren, Matthew Z. Madden, Diana C. Contreras, Debolanle O. Dahunsi, Jonathan M. Irish, Olalekan O. Oluwole, Jeffrey C. Rathmell, and Matthew H. Spitzer**

# Figure S1

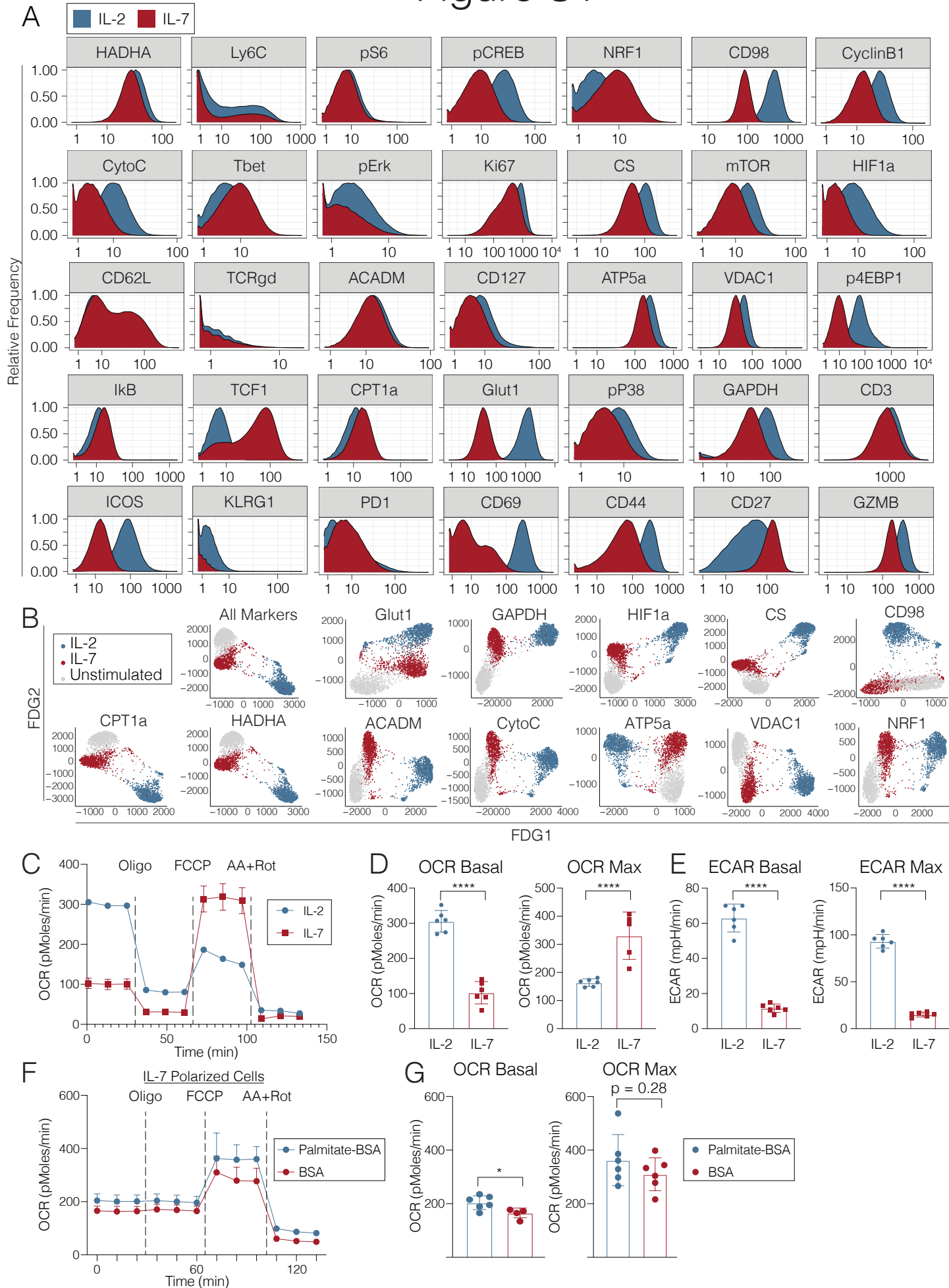


## **Figure S1**

**Assessing the integrated functional program of antigen specific CD8<sup>+</sup> T cell activation in vitro. Related to Figure 1.** (A) OT-1 transgenic CD8<sup>+</sup> T cells were stimulated with cognate peptide (SIINFEKL) in the presence of IL-2 (100U/ml) for 72 hours, followed by 3 washes to remove antigen and polarization in IL-2, IL-7 or IL-15 (all 10ng/mL) to generate OT-1<sub>eff</sub> or OT-1<sub>mem</sub>. Samples were fixed for mass cytometry at all time points depicted and cells were harvested at Day 7 for Seahorse assay analysis by Mitochondrial Stress Test. Mass cytometry expression data for key metabolic, signaling and effector markers of interest by histograms are displayed. (B) Force-directed graphs showing the relationships between single OT-1 T cells left unstimulated (gray) or stimulated and polarized with IL-2 (blue) or IL-7 (red), only taking into account the expression of metabolic proteins. Each metabolic protein is left out one at a time as indicated by the specific protein listed at the top of each figure panel. (C) OCR tracings depicting changes in OCR over time of OT-1 cells conditioned in IL-2 or IL-7. (D) Basal and maximal OCR readings and (E) basal and maximal ECAR readings as quantified by Seahorse. Significance analysis by paired two-tailed student's t-test ( $p<0.05$  \*,  $p<0.01$  \*\*,  $p=0.0001$ \*\*\*,  $p<0.0001$ \*\*\*\*). Error bars represent SEM. Data are representative of at least 2 independent experiments. (F) OCR tracings of OT-I T polarized in 10ng/ml IL-7 prior to incubation in FAO media for 15 minutes with the addition of either palmitate-BSA or BSA for extracellular analysis in the presence of 1.5  $\mu$ M Oligomycin, 1 $\mu$ M FCCP, and 0.5 $\mu$ M Antimycin A/Rotenone. Error bars represent SEM. (G) Basal and maximum OCR of OT-1 T cells subjected to palmitate oxidation assay as above. Significance analysis by student's t-test (\* $p<0.05$ ). Error bars represent SEM.

# Figure S2

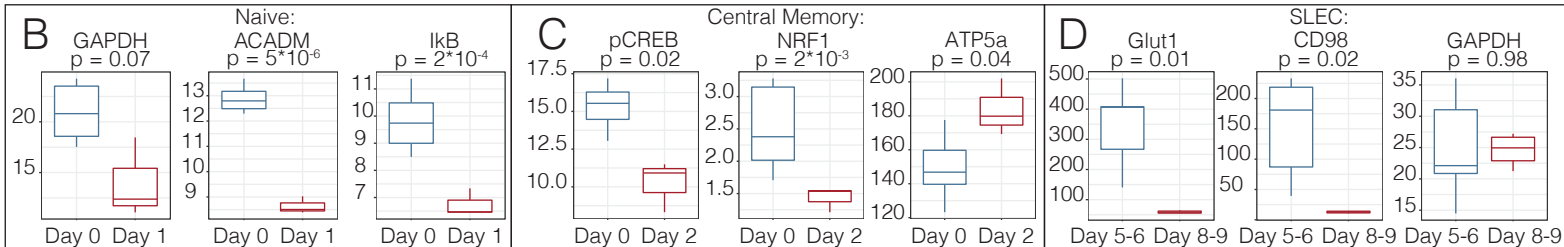
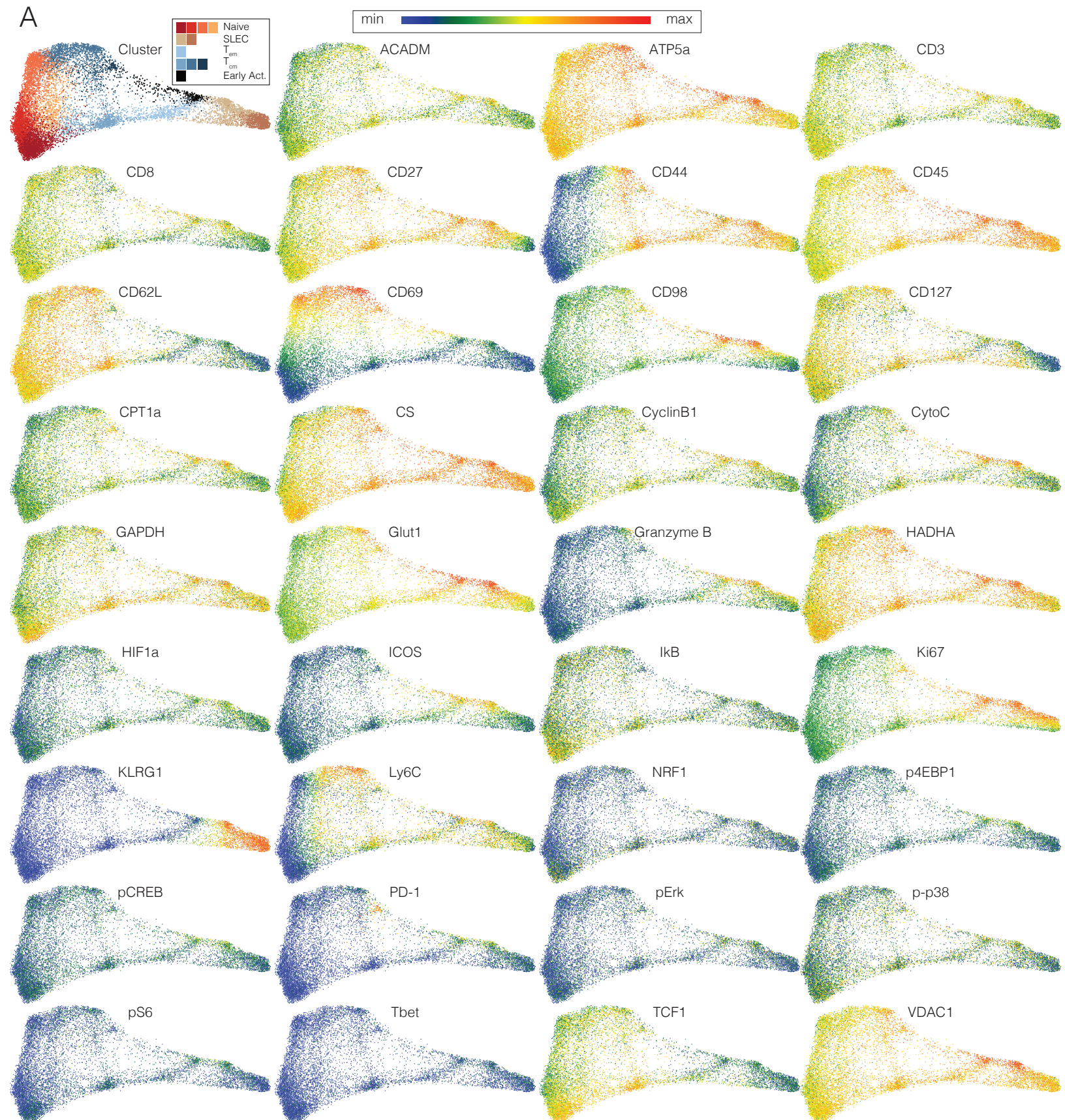
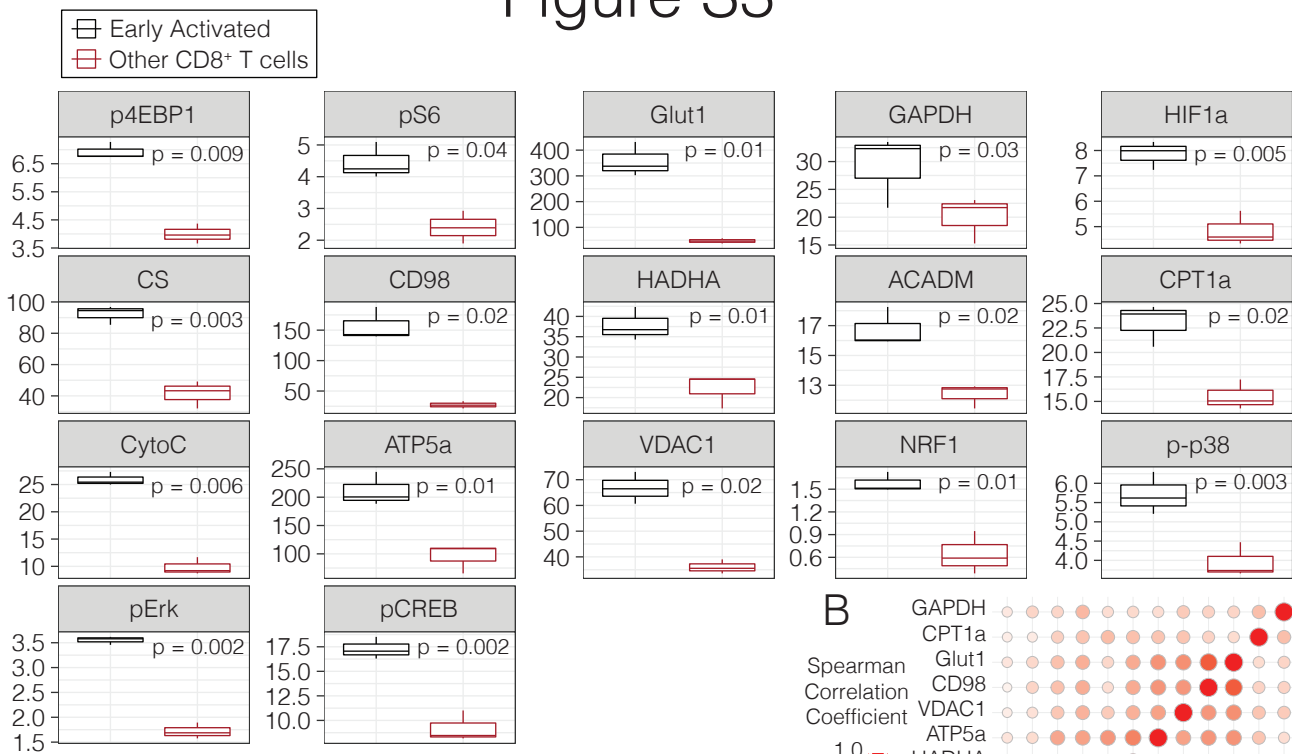


## **Figure S2**

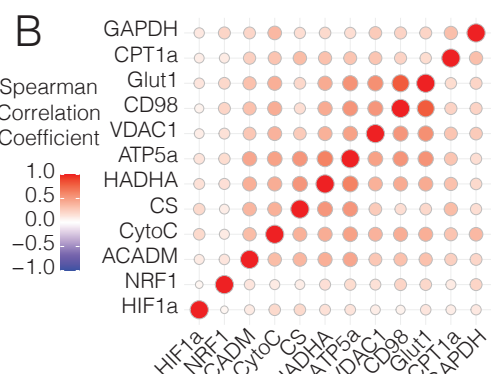
**Single-cell metabolic analysis of the primary CD8<sup>+</sup> T cell response in vivo. Related to Figure 2.** **(A)** Pooled CD8<sup>+</sup> T cells from mice at days 0 to 9 of Lm-OVA infection (n=2-3 mice per time point) clustered by Phenograph and visualized by force-directed graphs. Force-directed graphs of single-cell expression profiles of individual markers are depicted. Box plots of marker expression of **(B)** naïve, **(C)** central memory, and **(D)** SLECs at specified time points post-infection with Listeria monocytogenes. Significance analysis by paired two-tailed student's t-test. Whiskers represent 1.5 \* IQR.

# Figure S3

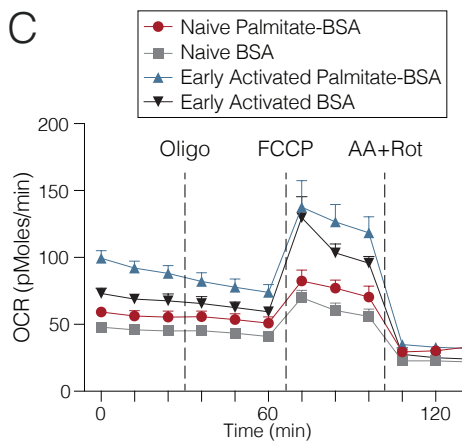
A



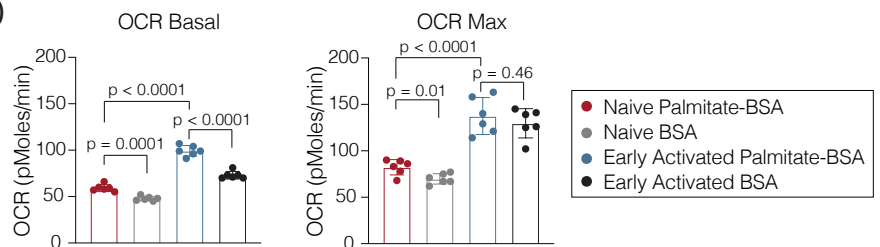
B



C



D



E

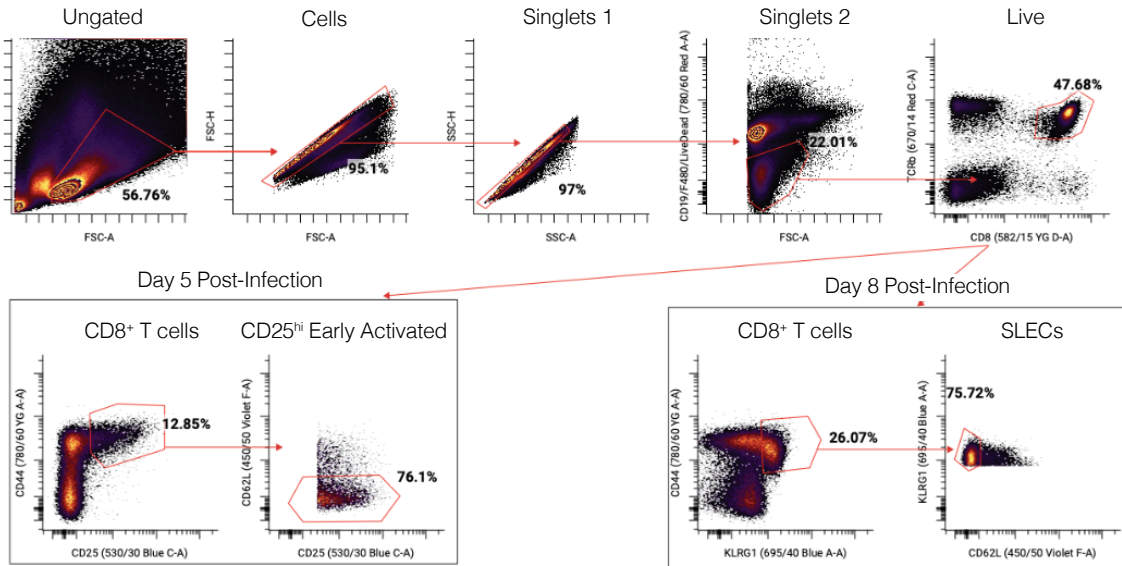


### **Figure S3**

**Single-cell metabolic analysis by mass cytometry reveals the unique metabolic profile of early activated CD8<sup>+</sup> T cells. Related to Figure 3.** **(A)** Box plots of marker expression of early activated T cells compared to all other CD8<sup>+</sup> T cells at day 5 p.i. with Listeria monocytogenes. Significance analysis by paired two-tailed student's t-test. Whiskers represent 1.5 \* IQR. **(B)** Spearman correlation matrix of markers in early activated CD8<sup>+</sup> T cells on day 5 p.i. **(C)** OCR tracings and **(D)** basal and maximal OCR readings of early activated or naïve T cells pooled and sorted from 20 mice at day 5 p.i. prior to incubation in FAO media for 15 minutes with the addition of either palmitate-BSA or BSA for extracellular analysis in the presence of 1.5 μM Oligomycin, 1μM FCCP, and 0.5μM Antimycin A/Rotenone. Error bars represent SEM. **(E)** Sorting strategy for isolation of naïve ( $CD62L^{hi}CD44^{low}KLRG1^{low}CD25^{lo}$ ), early activated cells ( $CD62L^{low}CD44^{hi}CD25^{hi}$ ) at day 5 post-infection and SLECs ( $CD62L^{low}CD44^{hi}KLRG1^{hi}CD25^{low}$ ) and day 8 post-infection is depicted by biaxial plots.

# Figure S4

A

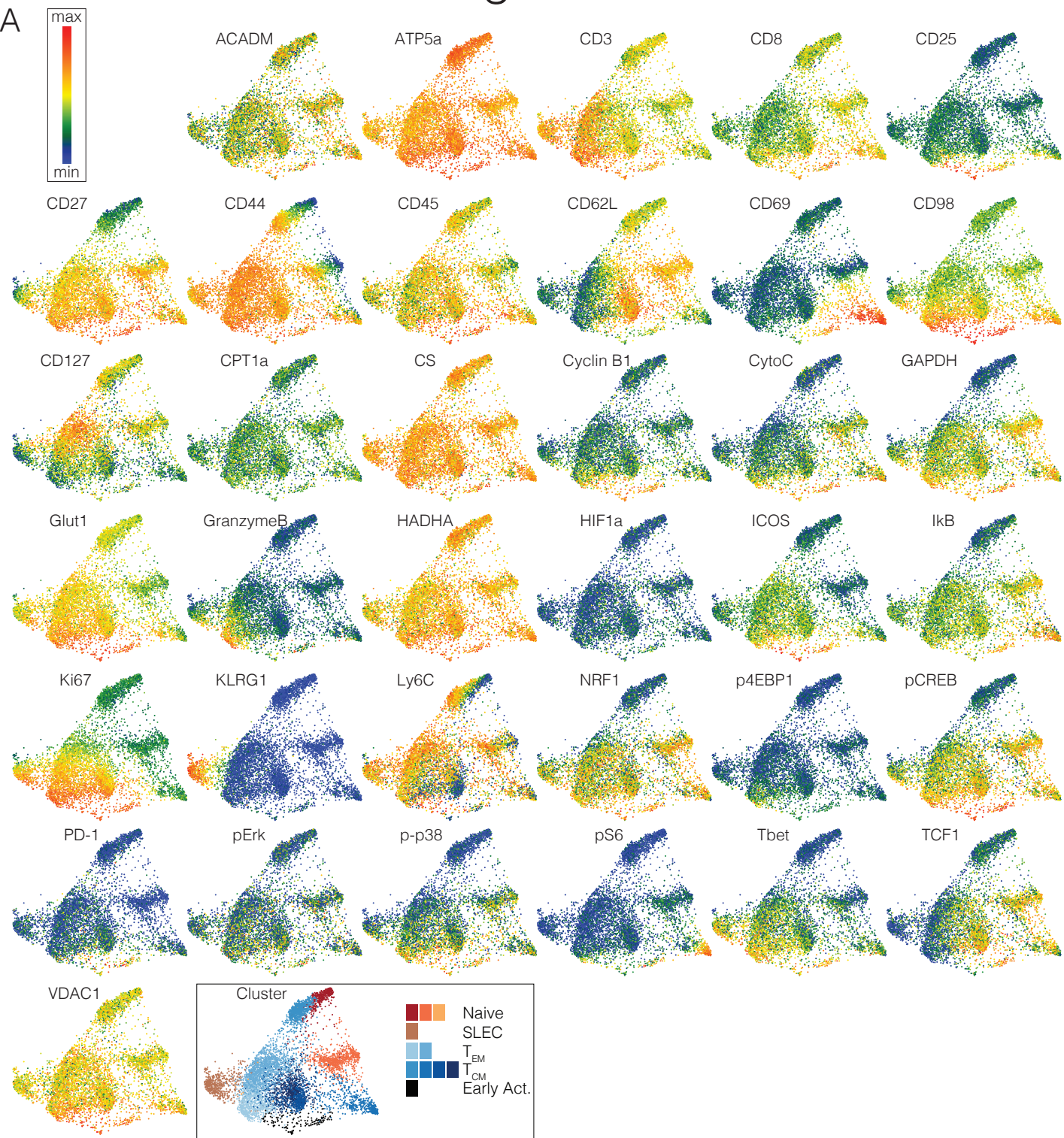


**Figure S4**

**Single-cell metabolic analysis of the antigen-specific primary CD8<sup>+</sup> T cell response in vivo.**

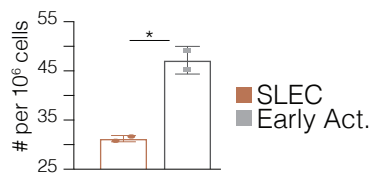
**Related to Figure 4. (A)** Pooled OT1 CD8<sup>+</sup> T cells from mice at days 3 to 7 of Lm-OVA infection

(n=1- 3 mice per time point) clustered by Phenograph and visualized by a force-directed graphs.

Force-directed graphs of single-cell expression profiles of individual markers are depicted.

# Figure S5

A



B

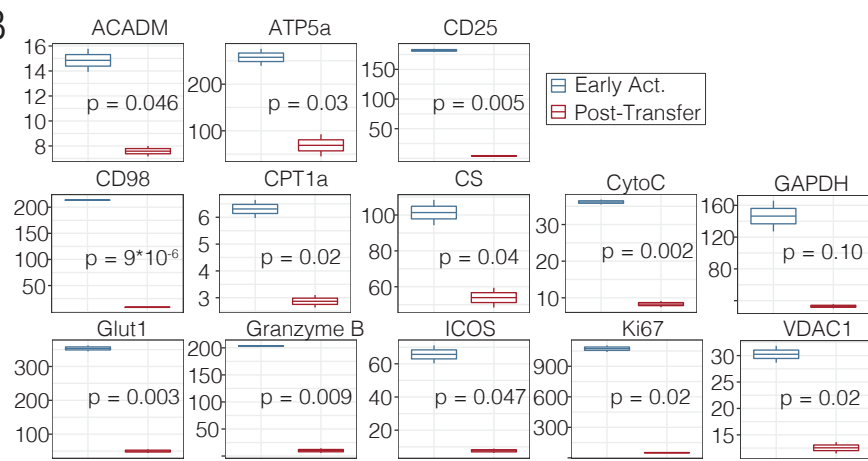


**Figure S5**

**The early activated T state is transient. Related to Figure 5.** **(A)** Number of congenic transferred cells derived from either early activated cells or SLECs four days after adoptive transfer. **(B)** Metabolic and signaling marker profiles of OT1 CD8<sup>+</sup> T cells before and after transfer at days 5 and 9 p.i. respectively are represented by histograms. Significance analysis by paired two-tailed student's t-test. Whiskers represent 1.5 \* IQR Significance analysis of the medians by two-tailed student's t-test ( $p<0.05$  \*,  $p<0.01$  \*\*) is displayed.

**Table S1**

**A mass cytometry panel targeting functional and phenotypic aspects of T cell differentiation for mouse and human studies. Related to STAR Methods.** Antibodies used in this study and their specifications are depicted in the table.

Channel	Marker	Vendor	Catalog No.	Clone	Species	[Optimal] (µg/ml)
89Y	Ter119	BioLegend	116202	TER-119	Mouse	6
113In	CD45.2	BioLegend	109802	104	Mouse	3
115In	CD45.1	BioLegend	110702	A20	Mouse	3
139La	CD4	BioLegend	100506	RMA4-5	Mouse	6
140Ce	CD8	BioLegend	100702	53-6.7	Mouse	6
141Pr	CD38	Biolegend	102702	90	Mouse	6
142Nd	HADHA	Abcam	ab231169	EPR17940	Mouse	6
143Nd	Ly6C	BioLegend	128002	HK1.4	Mouse	0.375
144Nd	pS6	CST	Custom	2F9	Mouse	3
145Nd	pCREB	CST	9198BF	87G3	Mouse	1.5
146Nd	NRF1	Abcam	ab221792	EPR5554(N)	Mouse	3
147Sm	CD98	BioLegend	128202	RL388	Mouse	3
148Nd	Cyclin B1	BD	Custom	GNS1	Mouse	6
149Sm	CytoC	BioLegend	612302	6H2.B4	Mouse	0.75
150Nd	T-bet	BioLegend	644802	4B10	Mouse	6
151Eu	pErk	CST	Custom	D13	Mouse	6
152Sm	Ki67	Thermo/eBioscience	11-5698-82	SolA15	Mouse	6
153Eu	CS	Abcam	ab233838	EPR8067	Mouse	0.75
154Sm	MTOR	CST	Custom	7C10	Mouse	6
155Gd	HIF1a	Thermo/Invitrogen	700505	16H4L13	Mouse	6
156Gd	CD62L	R&D	MAB5761	95218	Mouse	1.5
157Gd	TCRgd	BioLegend	118101	GL3	Mouse	1.5
158Gd	ACADM	Abcam	ab110296	3B7BH7	Mouse	6
159Tb	CD127	BioLegend	135002	A7R34	Mouse	6
160Gd	ATP5a	Abcam	ab110273	7H10BD4F9	Mouse	6
161Dy	VDAC1	Abcam	ab14734	20B12AF2	Mouse	6
162Dy	p4EBP1	CST	2855BF	236B4	Mouse	6
163Dy	ikBa	CST	4614BF	L35A5	Mouse	3
164Dy	TCF1/TCF7	CST	2203BF	C63D9	Mouse	6
165Ho	CPT1a	Abcam	ab128568	8F6AE9	Mouse	6
166Er	Glut1	Abcam	ab196357	EPR3915	Mouse	0.75
167Er	Foxp3	Thermo	Custom	NRRF-30	Mouse	3
168Er	p-p38	BD Pharmingen	Custom	36/p38	Mouse	1.5
168Er	CD25	BioLegend	102014	PC61	Mouse	3
169Tm	GAPDH	Thermo	AM4300	6C5	Mouse	1.5
170Er	CD3	BioLegend	100202	17A2	Mouse	3
171Yb	CD278/ICOS	BioLegend	313502	C398.4A	Mouse	3
172Yb	KLRG1	BioLegend	368602	2F1	Mouse	0.75
173Yb	PD1	BioLegend	135202	29F.1A12	Mouse	0.75
174Yb	CD69	R&D	AF2386	polyclonal	Mouse	6
175Lu	CD44	BioLegend	103002	IM7	Mouse	0.375
176Yb	CD27	BioLegend	124202	LG.3A10	Mouse	1.5
209Bi	Granzyme B	BioLegend	372202	QA16A02	Mouse	0.75
89Y	CD45	Fluidigm	3089003B	HI30	Human	2.5
141Pr	CD49d	Fluidigm	3141004B	9F10	Human	2.5
142Nd	TOX	Miltenyi	130-126-455	REA473	Human	5
143Nd	CD278/ICOS	Fluidigm	3143025B	C398.4A	Human	2.5

144Nd	ATP5a	Abcam	ab110273	7H10BD4F9	Human	2.5
145Nd	CAR	Kite Pharma	Custom	KIP3	Human	2.5
146Nd	CD197 (CCR7)	BioLegend	353237	G043H7	Human	2.5
	CD183 (CXCR3)	BioLegend	353733	G025H7	Human	2.5
147Sm	CPT1a	Abcam	ab128568	8F6AE9	Human	2.5
149Sm	CD29	BioLegend	303021	TS2/16	Human	1.25
150Nd	CD134 (OX40)	Fluidigm	3150023B	ACT35	Human	2.5
151Eu	Grim19	Abcam	ab110240	6E1BH7	Human	5
152Sm	CD95 (Fas)	Fluidigm	3152017B	DX2	Human	2.5
153Eu	HIF1a	CST	36169	D1S7W	Human	10
154Sm	TIM-3	Fluidigm	3154010B	F38-2E2	Human	2.5
155Gd	CD279 (PD-1)	Fluidigm	3155009B	EH12.2H7	Human	2.5
156Gd	Eomes	Miltenyi	81493BF	D8D1R	Human	5
158Gd	CD137/4-1BB	Fluidigm	3158013B	4B4-1	Human	2.5
159Tb	Glud1	Abcam	ab168352	EPR11370	Human	5
160Gd	XBP1s	CST	27901	E8C2Z	Human	5
161Dy	T-bet	Fluidigm	3161014B	4B10	Human	10
162Dy	CD27	Fluidigm	3162009B	L128	Human	2.5
163Dy	Glut1	Novus	NB110-39113	polyclonal	Human	1.25
164Dy	CytoC	BD	556432	6H2.B4	Human	0.625
165Ho	CD45RO	Fluidigm	3165011B	UCHL1	Human	2.5
166Er	CD28	BioLegend	302937	CD28.2	Human	2.5
167Er	TCF1	Miltenyi	2203BF	C63D9	Human	5
168Er	CD8a	Fluidigm	3168002B	SK1	Human	2.5
169Tm	CD45RA	Fluidigm	3169008B	HI100	Human	2.5
170Er	CD3	Fluidigm	3170001B	UCHT1	Human	2.5
171Yb	Granzyme B	Fluidigm	3171002B	GB11	Human	2.5
172Yb	Ki67	Fluidigm	3172024B	B56	Human	2.5
173Yb	CD223/LAG-3	BioLegend	369302	11C3C65	Human	2.5
174Yb	CD4	Fluidigm	3174004B	SK3	Human	2.5
175Lu	Perforin	Fluidigm	3175004B	B-D48	Human	5
176Yb	CD127	Fluidigm	3176004B	A019D5	Human	2.5